JOURNAL OF GUIDANCE, CONTROL, AND DYNAMICS
Vol. 45, No. 10, October 2022

Spacecraft Relative Motion Dynamics and Control Using Fundamental Modal Solution Constants

Ethan R. Burnett* and Hanspeter Schaub†
University of Colorado Boulder, Boulder, Colorado 80309

https://doi.org/10.2514/1.G006603

This paper explores expressing the relative state in the close-proximity satellite relative motion problem in terms of fundamental modal solution constants. The nominal uncontrolled relative state can be expressed in terms of a weighted sum of fundamental and geometrically insightful modal motions. These fundamental motions are obtained using the Lyapunov–Floquet theory. In the case that the dynamics are perturbed by the action of a controller or by unmodeled dynamics, the weights on each fundamental solution are allowed to vary as in a variation-of-parameters approach, and in this manner function as state variables. This methodology reveals interesting insights about satellite relative motion and enables elegant control approaches. This approach can be applied in any dynamical environment as long as the chief orbit is periodic, and this is demonstrated with results for relative motion analysis and control in the eccentric Keplerian problem and in the circular restricted three-body problem. Some commentary on the extension of the methodology beyond the periodic chief orbit case is also provided. This is a promising and widely applicable new approach to the close-proximity satellite relative motion problem.

I. Introduction

IN THE close-proximity relative motion control problem, the choice of coordinate representation greatly influences the ease of relative motion planning and design; and it can affect the complexity of feedback control development [1]. The traditional local relative Cartesian and spherical coordinate representations have proven to be quite popular [2], but there are other formulations that enable geometric approaches or provide great geometric insight into the influence of perturbations and control. Orbit element differences [3] and the related relative orbit element (ROE) formulations are important examples [4,5], and some missions have already implemented ROE formulations for relative motion control [6]. As opposed to a local coordinate formulation, depending on the choice of quantities, most or all orbit element differences or ROEs will be constants for uncontrolled Keplerian relative motion. In this sense, the unperturbed dynamics of relative motion are trivial in the orbit element differences, and the mapping from ROEs to other representations of the relative state can provide a local geometric interpretation [7]. These formulations also generally linearize quite well [8], which is a very useful feature.

Another relevant representation of relative motion was discussed in Ref. [9], which focused on the linearized relative orbit elements (LROEs) for the Clohessy–Wiltshire (CW) problem [10], and sought a representation with a straightforward geometric interpretation. This was accomplished by representing the CW solution in terms of the fundamental amplitude, phase, and offset quantities, which are themselves nonlinear functions of the initial relative state quantities in local Cartesian coordinates. These quantities are thus constant in the unperturbed problem in the absence of control. Given nonzero perturbations or control, these quantities vary in time, with their behavior given by equations obtained using a Lagrange–Bracket variational methodology [1]. There has also been some work relating integration constants for the CW problem to the ROE formulation. For example, Ref. [11] provided a mapping between the CW integration constants and the general ROEs.

Because the LROEs discussed in Ref. [9] were developed for CW dynamics, they are only appropriate for near-circular orbits and would not be appropriate for eccentric orbits. Additionally, the orbit element difference and ROE sets suffer from their own shortcomings. For example, they are not directly related to system observables [12]. Additionally, the application of any of these integral representations in highly non-Keplerian settings (such as in the three-body problem) would be cumbersome because, although they can still be a valid state representation via the variation of parameters, they are no longer nearly constant.

Motivated by the many benefits of integral relative state representations (such as the ROEs and LROEs) and by their shortcomings, this paper discusses an approach to modeling satellite relative motion dynamics and control that can be applied to the CW problem, the Keplerian problem with eccentricities of $0 < e < 1$, and beyond to the restricted three-body problems. This approach is called the *method of fundamental modal solutions*. The main idea of this work is that satellite relative motion can be represented as a weighted sum of fundamental solutions, which are chosen for maximal ease of geometric interpretation. This is accomplished by using the modal solutions previously developed by the authors through an application of the Lyapunov–Floquet theory [13], as well as more recent extensions. A benefit of this approach is that stable, unstable, oscillatory, and drift motions are naturally separated. In the absence of perturbation or control effort, the weights on each fundamental solution are constant. However, in the perturbed or controlled problem, the constants are made to vary through a variation-of-parameters framework such that the weighted sum of the fundamental solutions still always instantaneously describes the relative state. The collection of six time-varying weights serves as the state vector for the problem, and the benefits of this approach for dynamics, visualization, and control are discussed in this paper. This procedure is presently developed for close-proximity relative motion in the vicinity of any closed (periodic) chief orbit, regardless of the governing dynamics. To demonstrate its breadth of potential uses, the methodology is applied to the relative motion problem for Keplerian orbits of any eccentricity, as well as to orbits in the circular restricted three-body problem (CR3BP).

There are a few works that are particularly relevant to this paper due to their shared methods, mathematical techniques, and perspectives. First, this paper employs the Lyapunov–Floquet theory [14], for which the application to the relative motion problem has seen limited but noteworthy study. In Ref. [15], a Lyapunov–Floquet (LF) transformation relating the Clohessy–Wiltshire and Tschauner–Hempel dynamics was exploited for relative motion control design. Additionally, a simple LF transformation was used in Ref. [16] when

Presented as Paper 2022-2462 at the AIAA Scitech 2022 Forum, San Diego, CA, January 3–7, 2022; received 30 November 2021; revision received 15 April 2022; accepted for publication 24 May 2022; published online 30 August 2022.

*Ann and H.J. Smead Department of Aerospace Engineering Sciences, 431 UCB, Colorado Center for Astrodynamics Research.

†Glenn L. Murphy Chair of Engineering, Smead Department of Aerospace Engineering Sciences, 431 UCB, Colorado Center for Astrodynamics Research. Fellow AIAA.

incorporating the secular effect of the J_2 perturbation on orbit element differences. Recently, Ref. [17] devised a unified ROE–CW framework for close-proximity satellite relative motion control, adapting work from Ref. [11] and a periodic transformation between ROEs and local Cartesian coordinates for the CW problem. On the topic of the CR3BP, other works have previously explored formation flying in the Earth–moon three-body problem, particularly in the vicinity of the libration points. Past works, such as Refs. [18,19], are relevant.

The Keplerian modal decomposition discussed in this paper was first derived analytically in a recently published paper by the authors [13]. It is worth noting that there has been past exploration of the satellite relative motion problem using integration constants as state variables, or otherwise as quantities of interest. Reference [20] showed the first-order equivalence of the ROEs with the integration constants of the integrable homogeneous ordinary differential equation of relative motion for the CW case, and Refs. [21,22] showed similar equivalence for the Yamanaka–Ankerson case. Reference [5] showed that integration constants are useful as state variables for optimal control, and the control formulation explored in that paper is adopted for this work. Recently, Ref. [23] explored its application with Yamanaka–Ankersen integration constants to passive safe optimal satellite relative motion control on eccentric orbits.

This paper is organized as follows. First, the concept of the relative motion modal decomposition is introduced, and there is a brief review of the Lyapunov–Floquet transformation, which is used extensively in this work. The modal decomposition for general Keplerian orbits is introduced, which is applicable to any eccentricity of $0 < e < 1$. Then, the method of the variation of parameters is used to derive the dynamics of the modal constants for the case in which the chief orbit is perturbed from its reference periodic motion. Afterward, the theory is applied to relative motion in the vicinity of periodic orbits in the CR3BP, and an interesting parallel between the Keplerian close-proximity relative motion problem and its CR3BP counterpart is highlighted. Then, applications of the fundamental solution constants are discussed for modeling perturbed relative motion and for efficiently computing relative motion control policies. Finally, numerical results are shown for cases of both Keplerian and CR3BP dynamics. For the Keplerian case, the relative motion modes are computed and used to explore the design space of relative orbits; and the effect of J_2 on the Keplerian modes is explored. Then, fuel-optimal impulsive relative motion control using the modal decomposition is explored for both Keplerian relative motion and relative motion in the CR3BP, applying a state-of-the-art control approach introduced in Ref. [5]. The paper ends with a discussion of future work that would generalize this method to efficient relative motion analysis, modeling, and control in a wide variety of environments.

In summary, the three main contributions of this paper are as follows: First, the useful state representation in terms of the modal constants is introduced for Keplerian dynamics and for the CR3BP. This allows for an elegant and broadly applicable examination of the close-proximity satellite relative motion problem: from the CW and Tschauner–Hempel problems to relative motion in the CR3BP. Second, the satellite relative motion is studied via the decomposition in terms of the insightful fundamental modes. Third, the framework is applied to challenging dynamics scenarios, including spacecraft relative motion in eccentric orbits and the CR3BP dynamics.

II. Relative Motion Modal Decomposition

A. Theory and Fundamentals

In this work, close-proximity satellite relative motion is represented as a weighted sum of fundamental solutions:

$$\boldsymbol{x}(t) = \sum_{i=1}^{6} c_i \boldsymbol{\psi}_i(t) \tag{1}$$

Figure 1 illustrates this conceptually with a depiction of bounded planar relative motion decomposed into three simpler constituent modal motions.

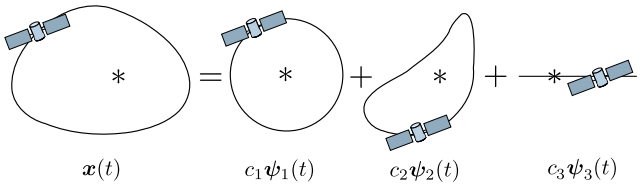

Fig. 1 Example satellite relative motion as a sum of individual modes.

The independent fundamental modal solutions $\boldsymbol{\psi}_i(t)$ form a complete functional basis for all possible close-proximity relative motion. The modal constants $\boldsymbol{c}$ are functions of the initial conditions $\boldsymbol{x}_0$ but, more generally, they can be treated as state variables. Consider the trivial example that the fundamental modal solutions are the columns of the state transition matrix $\boldsymbol{\psi}_i = \boldsymbol{\phi}_i$ and $\boldsymbol{c} = [\Phi(t_0, t_0)]^{-1}\boldsymbol{x}_0 = \boldsymbol{x}_0$. However, the columns of the state transition matrix are an inconvenient choice of functional basis, [13], and this paper uses a superior modal basis.

The modal decomposition is traditionally defined for autonomous linear dynamic systems, but all relative motion except the CW problem is characterized by nonautonomous differential equations. However, the Lyapunov–Floquet transformation [14] can be used to equate a linear time-varying (LTV) dynamic system with a periodic plant matrix of $[A(t)] = [A(t+T)]$ to a linear time-invariant (LTI) counterpart via a periodic coordinate transformation:

$$\boldsymbol{x} = [P(t)]z = [P(t+T)]z \tag{2}$$

where z represents the coordinate set for the LTI equivalent of the system in $\boldsymbol{x}$ with the following simple LTI dynamics:

$$\dot{z} = [\Lambda]z \tag{3}$$

The LF transformation and the LTI matrix are any pair of matrices $[P(t)]$ and $[\Lambda]$ satisfying the following matrix differential equation:

$$[P(t)]^{-1}([A(t)][P(t)] - [\dot{P}(t)]) = [\Lambda] \tag{4}$$

A unique definition of the LF transformation is given in the following using the monodromy matrix and the state transition matrix (STM). This transformation conveniently equals the identity at the epoch time:

$$[P(t)] = [\Phi(t, t_0)]e^{-[\Lambda](t-t_0)} \tag{5}$$

$$[P(t_0)] = [P(t_0 + kT)] = [I] \tag{6}$$

$$[\Lambda] = \frac{1}{T}\ln(\Phi(t_0 + T, t_0)) \tag{7}$$

The fundamental modal solutions in this work will thus be of the following form, assuming a diagonalizable LTI plant matrix $[\Lambda]$ with eigenvectors $\boldsymbol{v}_i$ and eigenvalues λ_i:

$$\boldsymbol{x}(t) = \sum_{i=1}^{6} c_i [P(t)]\boldsymbol{v}_i e^{\lambda_i t} \tag{8}$$

For the special case of purely Keplerian dynamics, $[\Lambda]$ has a Jordan form, and so the form of the modal decomposition is slightly modified from Eq. (8). From the condition where the plant matrix $[A(t)]$ is periodic, it is observed that this perspective applies for relative motion in the vicinity of any periodic chief orbit, regardless of the governing dynamics (two-body or three-body).

It is worth noting that there exists a simple linear mapping of the LF transformations and the resulting LTI matrices when two sets of coordinates are related by a linearized transformation. This relationship is demonstrated in the following for local coordinates $\boldsymbol{x}$ and orbit

element differences $\delta\boldsymbol{\alpha}$, which are approximately related by the linearized transformation $[G(t)]$:

$$\boldsymbol{x} = [G(t)]\delta\boldsymbol{\alpha} \tag{9}$$

$$[P_{\boldsymbol{x}}(t)] = [G(t)][P_{\delta\boldsymbol{\alpha}}(t)][G(t_0)]^{-1} \tag{10}$$

$$[\Lambda_{\boldsymbol{x}}] = [G(t_0)][\Lambda_{\delta\boldsymbol{\alpha}}][G(t_0)]^{-1} \tag{11}$$

See Ref. [1] for the linearized transformation $[G(t)]$. For this paper, $\delta\boldsymbol{\alpha}$ is in terms of the differential quasi-nonsingular orbit elements [1]:

$$\delta\boldsymbol{\alpha} = (\delta a, \delta\theta, \delta i, \delta q_1, \delta q_2, \delta\Omega)^{\top} \tag{12}$$

where $q_1 = e\cos\omega$, $q_2 = e\sin\omega$, $\theta = \omega + f$, and $\delta\boldsymbol{\alpha} = \boldsymbol{\alpha}_d - \boldsymbol{\alpha}_c$ is the deputy–chief orbit element difference.

Although there are many possible representations for satellite relative motion, this work mainly uses the popular local Cartesian coordinate representation. The relative state is the augmented relative position and velocity $\boldsymbol{x} = (\boldsymbol{\rho}^{\top}, \boldsymbol{\rho}'^{\top})^{\top}$ resolved in a chief-centered rotating coordinate frame called the Hill or local vertical/local horizontal (LVLH) frame as follows:

$$\boldsymbol{\rho} = x\hat{\boldsymbol{e}}_r + y\hat{\boldsymbol{e}}_t + z\hat{\boldsymbol{e}}_n \tag{13a}$$

$$\boldsymbol{\rho}' = \frac{{}^{H}\mathrm{d}}{\mathrm{d}t}(\boldsymbol{\rho}) = \dot{x}\hat{\boldsymbol{e}}_r + \dot{y}\hat{\boldsymbol{e}}_t + \dot{z}\hat{\boldsymbol{e}}_n \tag{13b}$$

The vector triad $\{\hat{\boldsymbol{e}}_r, \hat{\boldsymbol{e}}_t, \hat{\boldsymbol{e}}_n\}$ forming the LVLH frame is defined in the following in terms of the chief inertial position, velocity, and orbit angular momentum vectors $\boldsymbol{r}_c$, $\boldsymbol{v}_c$, and $\boldsymbol{h}_c$; and $(\,)'$ denotes the time derivative of quantities as seen in this frame:

$$\hat{\boldsymbol{e}}_r = \boldsymbol{r}_c/r_c \tag{14a}$$

$$\hat{\boldsymbol{e}}_n = \boldsymbol{h}_c/h_c \tag{14b}$$

$$\hat{\boldsymbol{e}}_t = \hat{\boldsymbol{e}}_n \times \hat{\boldsymbol{e}}_r \tag{14c}$$

The general dynamics in local Cartesian coordinates are given in terms of the chief radial vector $\boldsymbol{r}$, the angular velocity vector $\boldsymbol{\omega}$, and their derivatives in Ref. [24].

To facilitate the description of perturbed and controlled relative motions in terms of the Keplerian relative motion modes, the Keplerian modal decompositions are introduced. There are two of interest. The first is a straightforward solution to the LTI CW equations, and the second is a set of solutions to the general eccentric orbit case of $0 < e < 1$. Note that the CW problem is very simple and quite well studied, and similar factorizations of the CW system have previously appeared in the literature; see, e.g., Refs. [25,20]. Starting with the CW system, the full three-dimensional (3-D) modal decomposition is computed in the same fashion as its two-dimensional planar counterpart in Eqs. (11) and (12) in Ref. [13]:

$$\boldsymbol{x}_{\mathrm{CW}}(t) = \sum_{i=1}^{6} c_i \boldsymbol{\psi}_{i,\mathrm{CW}}(t) \tag{15}$$

$$[\Psi_{\mathrm{CW}}(t)] = \begin{bmatrix} 0 & -\frac{2}{3n} & -\frac{1}{n}\cos nt & \frac{1}{n}\sin nt & 0 & 0 \\ 1 & t & \frac{2}{n}\sin nt & \frac{2}{n}\cos nt & 0 & 0 \\ 0 & 0 & 0 & 0 & \frac{2}{n}\sin nt & \frac{2}{n}\cos nt \\ 0 & 0 & \sin nt & \cos nt & 0 & 0 \\ 0 & 1 & 2\cos nt & -2\sin nt & 0 & 0 \\ 0 & 0 & 0 & 0 & 2\cos nt & -2\sin nt \end{bmatrix} \tag{16}$$

$$\boldsymbol{c} = \begin{pmatrix} y_0 - \frac{2}{n}\dot{x}_0 \\ -6nx_0 - 3\dot{y}_0 \\ 3nx_0 + 2\dot{y}_0 \\ \dot{x}_0 \\ \frac{\dot{z}_0}{2} \\ \frac{n}{2}z_0 \end{pmatrix} \tag{17}$$

where c_i is the ith element of $\boldsymbol{c}$, and $\boldsymbol{\psi}_{i,\mathrm{CW}}(t)$ is the ith column of $[\Psi_{\mathrm{CW}}(t)]$. Because the CW system is already LTI, the LF transformation is just identity. Note that the typical modal decomposition of the CW plant matrix of $A = [V][J][V]^{-1}$ would produce complex $[V]$, and thus complex $\boldsymbol{c}$. This has been avoided for the derivation of Eq. (16), and it can generally always be avoided. Consider a pair of modes $\boldsymbol{\psi}_{m,n} = [P(t)]e^{\lambda_{m,n}t}\boldsymbol{v}_{m,n}$ with complex-conjugate eigenvalues λ_m and λ_n as well as eigenvectors $\boldsymbol{v}_m$ and $\boldsymbol{v}_n$. Taking the constants associated with the complex-conjugate modes c_m and c_n and defining new purely real constants $\tilde{c}_m = (c_m + c_n)/2$ and $\tilde{c}_n = (c_m - c_n)/2i$, their associated fundamental solutions will have a purely real form [13].

The preferred decomposition used in this paper for the general Keplerian case (any eccentricity of $0 < e < 1$) is the spherical coordinate modal decomposition, which is linearly mapped to Cartesian coordinates. This uses the argument of latitude of $\theta = \omega + f$ as the independent variable. The fundamental modal solutions consist of an along-track rectilinear motion, an offset circular mode, and only two geometrically nontrivial planar modes: a "teardrop" mode (changing from an initially elliptical shape to a highly pointed shape as eccentricity is increased from zero to one), and a drift mode. The Cartesian modal decomposition, by contrast, has three nontrivial planar modes. There are also two one-dimensional decoupled out-of-plane oscillatory modes. The spherical coordinate modal decomposition is given by the following equations [13], with $\boldsymbol{v}_i$ as columns of Eq. (24):

$$\begin{aligned}\boldsymbol{x}_{c(s)}(\theta) = {} & \sum_{i=1}^{5} c_i [F(\theta)]^{-1}[P_{\boldsymbol{x}_s}(\theta)]\boldsymbol{v}_i \\ & + c_6[F(\theta)]^{-1}[P_{\boldsymbol{x}_s}(\theta)](\boldsymbol{v}_5(\theta - \theta_0) + \boldsymbol{v}_6)\end{aligned} \tag{18}$$

$$[P_{\boldsymbol{x}_s}(\theta)] = [G_s(\theta)][P_{\delta\boldsymbol{\alpha}}(\theta)][G_s(\theta_0)]^{-1} \tag{19}$$

$$[P_{\delta\boldsymbol{\alpha}}(\theta)] = \begin{bmatrix} 1 & 0 & 0 & 0 & 0 & 0 \\ P_{21}(\theta) & P_{22}(\theta) & 0 & P_{24}(\theta) & P_{25}(\theta) & 0 \\ 0 & 0 & 1 & 0 & 0 & 0 \\ 0 & 0 & 0 & 1 & 0 & 0 \\ 0 & 0 & 0 & 0 & 1 & 0 \\ 0 & 0 & 0 & 0 & 0 & 1 \end{bmatrix} \tag{20}$$

$$P_{21}(\theta) = \frac{\kappa^2}{2a}(\mathbb{F}_{21}(\theta_0) - \mathbb{F}_{21}(\theta)) \tag{21a}$$

$$\begin{aligned}\mathbb{F}_{21}(\theta) = {} & \frac{6}{\eta^3}\left(\tan^{-1}\left(\frac{q_2 + (1 - q_1)\tan(\theta/2)}{\sqrt{1 - q_1^2 - q_2^2}}\right) - \frac{\theta}{2}\right) \\ & + \frac{3(q_2 + (q_1^2 + q_2^2)\sin\theta)}{q_1(q_1^2 + q_2^2 - 1)\kappa}\end{aligned} \tag{21b}$$

$$P_{22}(\theta) = \frac{\kappa^2}{\kappa_0^2} \tag{21c}$$

$$P_{24}(\theta) = \frac{\kappa^2}{4(q_1^2 + q_2^2 - 1)}(\mathbb{F}_{24}(\theta_0) - \mathbb{F}_{24}(\theta)) \tag{21d}$$

$$\mathbb{F}_{24}(\theta) = \frac{4(q_2 + \sin\theta)}{\kappa^2} + \frac{4\sin\theta}{\kappa} \tag{21e}$$

$$P_{25}(\theta) = \frac{\kappa^2}{4(q_1^2 + q_2^2 - 1)}(\mathbb{F}_{25}(\theta_0) - \mathbb{F}_{25}(\theta)) \tag{21f}$$

$$\mathbb{F}_{25}(\theta) = \frac{4(1 - q_1^2 + q_2 \sin\theta)}{q_1 \kappa^2} + \frac{4q_2 \sin\theta}{q_1 \kappa} \tag{21g}$$

$$[F(\theta)] = \begin{bmatrix} 1 & 0 & 0 & 0 & 0 & 0 \\ 0 & 1/r & 0 & 0 & 0 & 0 \\ 0 & 0 & 1/r & 0 & 0 & 0 \\ 0 & 0 & 0 & 1 & 0 & 0 \\ 0 & -\dot{r}/r^2 & 0 & 0 & 1/r & 0 \\ 0 & 0 & -\dot{r}/r^2 & 0 & 0 & 1/r \end{bmatrix} \tag{22}$$

$$[G_s(\theta)] = \begin{bmatrix} \frac{r}{a} & \frac{v_r}{v_t} r & 0 & -\frac{r}{p}(2aq_1 + r\cos\theta) & -\frac{r}{p}(2aq_2 + r\sin\theta) & 0 \\ 0 & 1 & 0 & 0 & 0 & \cos i \\ 0 & 0 & \sin\theta & 0 & 0 & -\cos\theta \sin i \\ -\frac{v_r}{2a} & \left(\frac{1}{r} - \frac{1}{p}\right)h & 0 & \frac{1}{p}(v_r a q_1 + h \sin\theta) & \frac{1}{p}(v_r a q_2 - h\cos\theta) & 0 \\ -\frac{3\dot{\theta}}{2a} & -2\frac{v_r}{r} & 0 & \frac{\dot{\theta}}{p}(3aq_1 + 2r\cos\theta) & \frac{\dot{\theta}}{p}(3aq_2 + 2r\sin\theta) & 0 \\ 0 & 0 & \dot{\theta}\cos\theta & 0 & 0 & \dot{\theta}\sin\theta\sin i \end{bmatrix} \tag{23}$$

$$[V_{R_{x_s}}] = \begin{bmatrix} 0 & 0 & 0 & 0 & \frac{2R_{21}a}{\gamma} AC\gamma a & 0 \\ 1 & 0 & 0 & 0 & \frac{2R_{21}a}{\gamma}(B+1)^2 C & 0 \\ 0 & 1 & 0 & 0 & 0 & 0 \\ 0 & 0 & 1 & 0 & \frac{2R_{21}a}{\gamma} B\gamma a & 0 \\ 0 & 0 & -\frac{A}{\gamma a} & 0 & -\frac{4R_{21}a}{\gamma} A(B+1) & 1 \\ 0 & 0 & 0 & 1 & 0 & 0 \end{bmatrix} \tag{24}$$

In the preceding equations, $v_r = \dot{r}$ and $v_t = r\dot{\theta}$, and $q_1 = e\cos\omega$, $q_2 = e\sin\omega$. The remaining quantities are defined as follows:

$$R_{21} = -\frac{3a\eta}{2r_0^2} \tag{25a}$$

$$A = q_2\cos\theta_0 - q_1\sin\theta_0 \tag{25b}$$

$$B = q_1\cos\theta_0 + q_2\sin\theta_0 \tag{25c}$$

$$C = \frac{hr_0^2}{a\mu\gamma} \tag{25d}$$

$$\gamma = A^2 + B^2 - 1 \tag{25e}$$

$$\eta = \sqrt{1 - q_1^2 - q_2^2} \tag{25f}$$

$$\kappa = 1 + q_1\cos\theta + q_2\sin\theta \tag{25g}$$

$$\kappa_0 = 1 + q_1\cos\theta_0 + q_2\sin\theta_0 \tag{25h}$$

The fundamental solution constants, which are quite important, are given in terms of initial spherical relative coordinates by Eq. (26):

$$c_1 = -\frac{v_{t,0}}{v_{r,0} r}\delta r_0 + \theta_{r,0} \tag{26a}$$

$$c_2 = \phi_{r,0} \tag{26b}$$

$$c_3 = \frac{1}{C}\left(\frac{(1 - (r_0/p))v_{t,0}}{v_{r,0}}\delta r_0 + C\delta\dot{r}_0\right) \tag{26c}$$

$$c_4 = \dot{\phi}_{r,0} \tag{26d}$$

$$c_5 = -\frac{v_{t,0}}{3v_{r,0}a} n\left(\frac{r_0}{p}\right)\delta r_0 \tag{26e}$$

$$c_6 = \frac{\mu}{hr_0^2}\left(1 + \frac{p}{r_0}\right)\delta r_0 + \frac{v_{r,0}}{v_{t,0} r_0}\delta\dot{r}_0 + \dot{\theta}_{r,0} \tag{26f}$$

The function $[F(\theta)]$ linearly maps the Cartesian coordinates x, y, z, $\dot{x}$, $\dot{y}$, and $\dot{z}$ to the spherical relative state coordinates δr, θ_r, ϕ_r, $\delta\dot{r}$, $\dot{\theta}_r$, and $\dot{\phi}_r$, and it can be used for getting the spherical coordinate initial conditions required by Eq. (26). Note that singularities exist with the given Keplerian modal formulation, appearing when $q_1 = e\cos\omega = 0$ or when $e\sin f_0 = 0$. These can be avoided by selecting nearby conditions, setting the offending terms to a small number ϵ instead of exactly zero.

The modal decompositions can always be normalized to maximize ease in geometric interpretation of the relative scales of the c_i:

$$\boldsymbol{x}(t) = \sum_{i=1}^{6} c_i \boldsymbol{\psi}_i(t) = \sum_{i=1}^{6} c_i \|\boldsymbol{\psi}_i\| \hat{\boldsymbol{\psi}}_i(t) = \sum_{i=1}^{6} \bar{c}_i \hat{\boldsymbol{\psi}}_i(t) \tag{27}$$

where the choice of normalization is left to the reader. A simple choice is to make it so that the maximum relative range of a normalized mode over the course of one orbit is unity. This is the standard normalization scheme applied for all results in this paper.

The normalized planar (x and y) modes for the linearly mapped spherical coordinates are produced in Fig. 2 for an example case with an unperturbed chief orbit about Earth with elements of $a =$ 12,000 km, $e = 0.4$, $i = 25$ deg, $\Omega = 0$ deg, $\omega = 270.001$ deg, and $f_0 = 90$ deg. The initial points for each mode are indicated

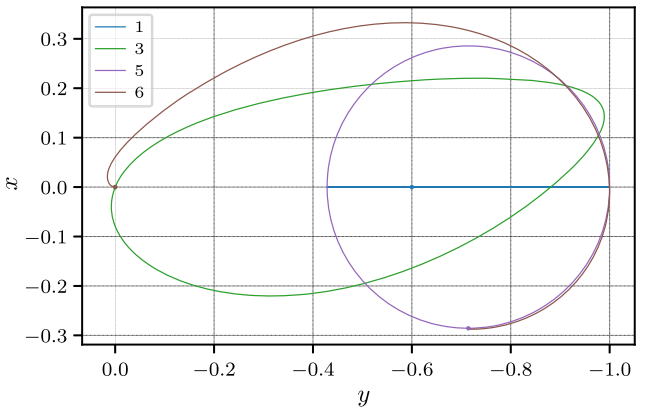

Fig. 2 Example in-plane normalized relative motion modes.

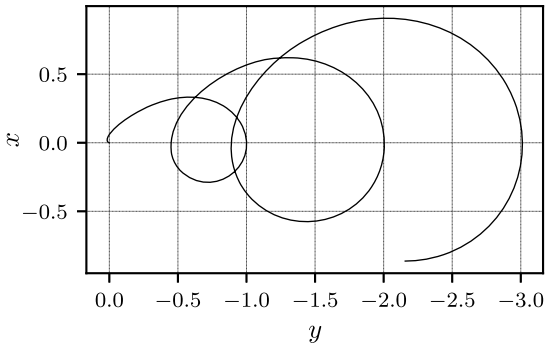

Fig. 3 Drift mode: three orbits.

with a dot. The out-of-plane modes, which are simply linearly independent oscillations in z, are not shown. From Fig. 2, the planar projection of all close-proximity unperturbed relative motion in this case is revealed to be a linear sum of geometrically simple independent motions. The first is an along-track oscillation (mode 1, shown flipped about $y = 0$ for convenience), a distorted teardrop mode (mode 3), an offset circle mode (mode 5), and a drift mode (mode 6). Note that the chief eccentricity dictates the ratio of the offset circle's radius to its distance from the origin, and the along-track oscillation of mode 1 has the same maximum and minimum y bounds as the offset circle mode. Note also that the drift mode behaves as a composition of a secularly expanding mode 5 and a translation along the y axis; see the last term in Eq. (18). To better illustrate this behavior, the drift mode is shown for three chief orbit periods in Fig. 3. Although the uncontrolled state evolves as a sum of the modes, the state can be uniquely parameterized by the stationary $\boldsymbol{c}$ and the time since epoch $t - t_0$. In this sense, the modal solution constants function similarly to orbit elements but with the exact linear mapping of $\boldsymbol{x}(t) = [\Psi(t)]\boldsymbol{c}$ to local relative state coordinates. There are many possible alternate choices of fundamental solutions $\boldsymbol{\psi}_i(t)$, but the Lyapunov–Floquet theory is typically useful for identifying geometrically favorable solutions. It is worth noting that the use of the modal decomposition approach is not limited to Keplerian dynamics. This method can be applied to study motion in the vicinity of any periodic orbit (and work is ongoing to extend this to the more general case of a quasi-periodic chief orbit). This will be shown with an application of the method to the relative motion problem in the circular restricted three-body problem.

B. Modal Constants as State Variables

For the Keplerian problem, any uncontrolled close-proximity relative motion $\boldsymbol{x}(t)$ can be expressed as a constant weighted sum of the fundamental modal motions. In the event that the orbital dynamics are perturbed, or control is active, the general behavior can still be represented by a time-varying weighted sum of the modal motions:

$$\dot{\boldsymbol{x}} = \boldsymbol{f}(\boldsymbol{x}, \boldsymbol{u}, t) \tag{28a}$$

$$\boldsymbol{x}(t) = [\Psi(t)]\boldsymbol{c}(t) \tag{28b}$$

where the first equation gives the general true nonlinear dynamics, and $\boldsymbol{c}(t)$ is made to vary such that these dynamics are satisfied. The vector of constants is allowed to vary in time as $\boldsymbol{c}(t)$ such that any motion $\boldsymbol{x}(t)$ can be represented. This is enabled by the following osculating condition:

$$\dot{\boldsymbol{x}}(t) = \frac{\partial \boldsymbol{x}}{\partial t} + \frac{\partial \boldsymbol{x}}{\partial \boldsymbol{c}}\dot{\boldsymbol{c}} = \boldsymbol{f}(\boldsymbol{x}, \boldsymbol{u}, t) \tag{29a}$$

$$\frac{\partial \boldsymbol{x}}{\partial t} = [A(\boldsymbol{\alpha}^*, t)]\boldsymbol{x} \tag{29b}$$

where $[A(\boldsymbol{\alpha}^*, t)]$ is the plant matrix for the original linearized dynamics used to compute the fundamental modal solutions $[\Psi(t)]$. The new quantity $\boldsymbol{u}$ is the control signal, which in this paper is composed of the LVLH components of the thrust acceleration of the deputy spacecraft, i.e., $\boldsymbol{u} = {}^H(a_x, a_y, a_z)^\top$. The following dynamics satisfy the osculating condition:

$$\dot{\boldsymbol{c}} = [\Psi(t)]^{-1}(\boldsymbol{f}(\boldsymbol{x}, \boldsymbol{u}, t) - [A(\boldsymbol{\alpha}^*, t)]\boldsymbol{x}) \tag{30}$$

Assuming that $\boldsymbol{x}(t)$ remains in the linear regime, Eq. (30) reduces to linear dynamics in $\boldsymbol{c}$:

$$\dot{\boldsymbol{c}} = [\Psi(t)]^{-1}\Big([A(t)] - [A^*(t)]\Big)[\Psi(t)]\boldsymbol{c} + [\Psi(t)]^{-1}[B_x]\boldsymbol{u} \tag{31}$$

where $[B_x] = [0_{3\times3}\ I_{3\times3}]^\top$ if $\boldsymbol{x}$ is in Cartesian coordinates, and $[A(t)]$ is the plant matrix for linearization about the true (deviated) chief orbit. In the case that the orbital dynamics are unchanged, Eq. (31) obtains a form where $\boldsymbol{c}$ is only influenced by control:

$$\dot{\boldsymbol{c}} = [\Psi(t)]^{-1}[B_x]\boldsymbol{u} \tag{32}$$

Because $\boldsymbol{c}$ has no linearized plant matrix, it is possible in this case to design control to track a desired natural reference trajectory $\boldsymbol{x}_r(t)$ using a regulation controller in $\boldsymbol{c}$ space because the dynamics of the error $\delta\boldsymbol{c} = \boldsymbol{c} - \boldsymbol{c}_r$ are of the same form as Eq. (32).

In the case that the true orbit is weakly perturbed in comparison to the orbit used to develop the modal decomposition, one may write the true plant matrix in terms of the nominal plus a small deviation:

$$[A(t)] \approx [A^*(t)] + \varepsilon[\delta\tilde{A}(t)] \tag{33}$$

where $|\varepsilon| \ll 1$ is a small parameter. In this case, Eq. (31) is rewritten:

$$\begin{aligned}\dot{\boldsymbol{c}} &= \varepsilon[\Psi(t)]^{-1}[\delta\tilde{A}(t)][\Psi(t)]\boldsymbol{c} + [\Psi(t)]^{-1}[B_x]\boldsymbol{u} \\ &\equiv \varepsilon[\Omega(t)]\boldsymbol{c} + [B_c(t)]\boldsymbol{u}\end{aligned} \tag{34}$$

Equation (34) is interesting because as the relative state is written as $\boldsymbol{x}(t) = [\Psi(t)]\boldsymbol{c}(t)$, the perturbed close-proximity dynamics of relative motion can be factored into a traditional slow/fast dynamical system:

$$[\dot{\Psi}] = [A^*(t)]\Psi \tag{35a}$$

$$\dot{\boldsymbol{c}} = \varepsilon[\Omega(t)]\boldsymbol{c} + [B_c(t)]\boldsymbol{u} \tag{35b}$$

where from Eq. (34), the matrices $[\Omega]$ and $[B_c]$ are also functions of the modal solutions. The "slowness" of the dynamics in $\boldsymbol{c}$ implies that for weakly perturbed cases, the state $\boldsymbol{c}(t)$ will change slowly from $\boldsymbol{c}(t_0)$ in comparison to how the $\boldsymbol{\psi}_i(t)$ change from $\boldsymbol{\psi}_i(t_0)$ and how $\boldsymbol{x}(t)$ changes from $\boldsymbol{x}(t_0)$. This allows interpretation of the evolving relative motion using the osculating modal constants, which is similar to how the osculating orbital elements are used to study general perturbed satellite orbits.

C. Extension to the Circular Restricted Three-Body Problem

Equations (1–8) apply for relative motion in the vicinity of any periodic orbit, and not just in the Keplerian case. Thus, this paper explores relative motion in the circular restricted three-body problem from the same perspective. For this problem, the states and time are nondimensionalized in the traditional manner [26], with dynamics resolved in the rotating coordinates in which the two primaries appear fixed. The relative motion in the vicinity of a periodic orbit is studied in CR3BP rotating coordinates and is given as $\delta\boldsymbol{x} = [P(\tau)]\boldsymbol{z}$ (where the delta differentiates this from the usual LVLH frame relative state) and $\dot{\boldsymbol{z}} = [\Lambda]\boldsymbol{z}$.

Due to the Hamiltonian nature of the CR3BP, the monodromy matrix has a repeated eigenvalue of $\lambda_{m,1} = \lambda_{m,2} = +1$. Furthermore, it can be shown that the state rate $\dot{\boldsymbol{X}}(\tau_0) = \dot{\boldsymbol{X}}(\tau_0 + T)$ is an eigenvector corresponding to the unity eigenvalue. There is not a second eigenvector; the unity eigenvalue has algebraic multiplicity of two and

geometric multiplicity of one. Solving for the generalized eigenvector $\boldsymbol{v}_2$ is straightforward:

$$([\Phi(\tau_0 + T, \tau_0)] - [I_{6\times 6}])\boldsymbol{v}_2 = \boldsymbol{v}_1 \tag{36}$$

Then, the resulting Jordan decomposition of the monodromy matrix is as follows:

$$[\Phi(\tau_0 + T, \tau_0)] = [V_m][J_m][V_m]^{-1} = [\boldsymbol{v}_1\boldsymbol{v}_2 \ldots \boldsymbol{v}_6]\begin{bmatrix} 1 & 1 & 0 & \ldots \\ 0 & 1 & 0 & \ldots \\ 0 & 0 & \lambda_{m,3} & \\ \vdots & \vdots & & \ddots \end{bmatrix}[\boldsymbol{v}_1\boldsymbol{v}_2 \ldots \boldsymbol{v}_6]^{-1} \tag{37}$$

The LTI matrix is given by $[\Lambda] = (1/T)\ln(\Phi(\tau_0 + T, \tau_0))$:

$$[\Lambda] = \frac{1}{T}[V_m]\ln(J_m)[V_m]^{-1} = \frac{1}{T}[\boldsymbol{v}_1\boldsymbol{v}_2 \ldots \boldsymbol{v}_6]\begin{bmatrix} 0 & 1 & 0 & \ldots \\ 0 & 0 & 0 & \ldots \\ 0 & 0 & \ln(\lambda_{m,3}) & \\ \vdots & \vdots & & \ddots \end{bmatrix}[\boldsymbol{v}_1\boldsymbol{v}_2 \ldots \boldsymbol{v}_6]^{-1} \tag{38}$$

The solution to linearized relative motion in the CR3BP has the following form, with a drift mode as a result of the defectiveness:

$$\delta\boldsymbol{x}(\tau) = c_1[P(\tau)]\boldsymbol{v}_1 + c_2[P(\tau)](\boldsymbol{v}_1\tau + \boldsymbol{v}_2) + c_3\boldsymbol{\psi}_3(\tau) + \cdots + c_6\boldsymbol{\psi}_6(\tau) \tag{39}$$

where the trivial mode is the first listed mode, being periodic in CR3BP coordinates; and the drift mode is listed second. Then, there are four other modes (stable, unstable, or center) starting with $\boldsymbol{\psi}_3$. Recall that the delta notation is adopted for the CR3BP case to differentiate these differential CR3BP coordinates from the LVLH coordinates in the Keplerian case.

The defectiveness of the LTI form, its double-zero eigenvalues, and the resulting secular drift mode might remind the reader of the Keplerian relative motion modal decomposition. The drift mode has a simple physical interpretation: bounded relative motion must satisfy a period-matching condition, and so motion on the nearby orbits of different periods would violate this condition and result in nonzero projection into a local drift mode in the linearized system. This relationship also appears in the Keplerian relative motion problem: bounded purely along-track relative motion is possible (representing points of a different phase along the orbit); and in the case in which the no-drift condition is violated, the drift occurs along this same along-track direction.

The preceding discussion of the defectiveness of the monodromy matrix (and the underlying LTI form) and the resulting drift mode enables a fully analytic view of the relative motion modes. First, consider the case of relative motion in the vicinity of a stable orbit, where all the relative motion modes are bounded (i.e., all eigenvalues of $[\Lambda]$ have zero real parts). In this case, there is one pair of trivial eigenvalues and there are two nontrivial pairs of eigenvalues:

$$\lambda_{1,2} = 0 \tag{40a}$$

$$\lambda_{3,4} = \pm i\omega_1 \tag{40b}$$

$$\lambda_{5,6} = \pm i\omega_2 \tag{40c}$$

Let the complex-conjugate eigenvector pairs associated with the frequencies ω_1 and ω_2 be written as $\boldsymbol{v}_{3,4} = \boldsymbol{v}_{\mathbb{R}_1} \pm i\boldsymbol{v}_{\mathbb{I}_1}$ and $\boldsymbol{v}_{5,6} = \boldsymbol{v}_{\mathbb{R}_2} \pm i\boldsymbol{v}_{\mathbb{I}_2}$, respectively. Refactoring, the following form is obtained for the modal decomposition of the relative motion:

$$\delta\boldsymbol{x}(\tau) = \sum_{i=1}^{6} c_i\boldsymbol{\psi}_i(\tau) \tag{41a}$$

$$\boldsymbol{\psi}_i = [P(\tau)]\boldsymbol{\eta}_i(\tau) \tag{41b}$$

$$\boldsymbol{\eta}_1(\tau) = \boldsymbol{v}_1 \tag{42a}$$

$$\boldsymbol{\eta}_2(\tau) = \boldsymbol{v}_1\tau + \boldsymbol{v}_2 \tag{42b}$$

$$\boldsymbol{\eta}_3(\tau) = 2(\boldsymbol{v}_{\mathbb{R}_1}\cos(\omega_1\tau) - \boldsymbol{v}_{\mathbb{I}_1}\sin(\omega_1\tau)) \tag{42c}$$

$$\boldsymbol{\eta}_4(\tau) = -2(\boldsymbol{v}_{\mathbb{R}_1}\sin(\omega_1\tau) + \boldsymbol{v}_{\mathbb{I}_1}\cos(\omega_1\tau)) \tag{42d}$$

$$\boldsymbol{\eta}_5(\tau) = 2(\boldsymbol{v}_{\mathbb{R}_2}\cos(\omega_2\tau) - \boldsymbol{v}_{\mathbb{I}_2}\sin(\omega_2\tau)) \tag{42e}$$

$$\boldsymbol{\eta}_6(\tau) = -2(\boldsymbol{v}_{\mathbb{R}_2}\sin(\omega_2\tau) + \boldsymbol{v}_{\mathbb{I}_2}\cos(\omega_2\tau)) \tag{42f}$$

where the $\boldsymbol{c}$ is given as a function of $\delta\boldsymbol{x}_0$:

$$\boldsymbol{c} = [\bar{V}]^{-1}\delta\boldsymbol{x}_0 \tag{43}$$

$$[\bar{V}] = \left[\boldsymbol{v}_1, \boldsymbol{v}_2, 2\boldsymbol{v}_{\mathbb{R}_1}, -2\boldsymbol{v}_{\mathbb{I}_1}, 2\boldsymbol{v}_{\mathbb{R}_2}, -2\boldsymbol{v}_{\mathbb{I}_2}\right] \tag{44}$$

Because modes $\boldsymbol{\psi}_3$–$\boldsymbol{\psi}_6$ are generally composed of multiple incommensurate frequencies, they trace out complex and unintuitive shapes on long time spans. The trivial modes associated with the double-zero eigenvalues of $[\Lambda]$ are comparatively simple because they are T periodic. Together, these modes form the basis of all close-proximity relative motion in the vicinity of the periodic orbit. Another example is the case of two trivial modes, two center modes, a stable mode, and an unstable mode. The modal decomposition is given as follows, where $\boldsymbol{v}_{3,4} = \boldsymbol{v}_{\mathbb{R}_1} \pm i\boldsymbol{v}_{\mathbb{I}_1}$:

$$\delta\boldsymbol{x}(\tau) = \sum_{i=1}^{6} c_i\boldsymbol{\psi}_i(\tau) \tag{45a}$$

$$\boldsymbol{\psi}_i = [P(\tau)]\boldsymbol{\eta}_i(\tau) \tag{45b}$$

$$\boldsymbol{\eta}_1(\tau) = \boldsymbol{v}_1 \tag{46a}$$

$$\boldsymbol{\eta}_2(\tau) = \boldsymbol{v}_1\tau + \boldsymbol{v}_2 \tag{46b}$$

$$\boldsymbol{\eta}_3(\tau) = 2(\boldsymbol{v}_{\mathbb{R}_1}\cos(\omega_1\tau) - \boldsymbol{v}_{\mathbb{I}_1}\sin(\omega_1\tau)) \tag{46c}$$

$$\boldsymbol{\eta}_4(\tau) = -2(\boldsymbol{v}_{\mathbb{R}_1}\sin(\omega_1\tau) + \boldsymbol{v}_{\mathbb{I}_1}\cos(\omega_1\tau)) \tag{46d}$$

$$\boldsymbol{\eta}_5(\tau) = \boldsymbol{v}_5 e^{\lambda_5\tau} \tag{46e}$$

$$\boldsymbol{\eta}_6(\tau) = \boldsymbol{v}_5 e^{\lambda_6\tau} \tag{46f}$$

$$[\bar{V}] = [\,\boldsymbol{v}_1,\ \boldsymbol{v}_2,\ 2\boldsymbol{v}_{\mathbb{R}_1},\ -2\boldsymbol{v}_{\mathbb{I}_1},\ \boldsymbol{v}_5,\ \boldsymbol{v}_6\,] \tag{47}$$

In this case, the existence of an unstable mode generally results in relative motion being unstable if there is any projection of $\delta\boldsymbol{x}$ into the unstable subspace. All other dynamic cases can be explored as needed in the same manner as the preceding two cases.

III. Applications of the Fundamental Solution Constants

A. Analytic Benefits as a State Representation

For researchers interested in approximating satellite relative motion efficiently, it is worth noting that first-order perturbative expansions [27,28] of the perturbed relative motion in $\boldsymbol{c}$ space are quite convenient in comparison to the typical investigations in $\boldsymbol{x}$ space or in $\delta\boldsymbol{\alpha}$ coordinates:

$$\dot{\boldsymbol{c}} = \varepsilon[\Omega(t)]\boldsymbol{c} \tag{48}$$

$$\boldsymbol{c}(t) \approx \boldsymbol{c}^0 + \varepsilon\boldsymbol{c}^1(t) \tag{49}$$

$$\dot{\boldsymbol{c}}^1 = [\Omega(t)]\boldsymbol{c}^0 \tag{50}$$

where $\boldsymbol{c}^0$ is the unperturbed (zeroth-order) vector of constants, and the first-order correction $\boldsymbol{c}^1(t)$ induced by the linearized perturbation $[\Omega(t)]$ [see Eq. (34)] is solved simply by integration. Then, $\boldsymbol{x}$ is expanded in terms of the perturbed $\boldsymbol{c}$:

$$\boldsymbol{c}^1(t) = \int_0^t [\Omega(\varphi)]\,\mathrm{d}\varphi\boldsymbol{c}^0 \tag{51}$$

$$\boldsymbol{x}(t) \approx [\Psi(t)]\left([I_{6\times 6}] + \varepsilon\int_0^t [\Omega(\varphi)]\,\mathrm{d}\varphi\right)[\Psi(0)]^{-1}\boldsymbol{x}_0 \tag{52}$$

B. Continuous Control Using the Fundamental Solution Constants

In the classical linear quadratic tracking (LQT) problem, the formulation in terms of local coordinates (such as the Cartesian representation) is inconvenient. To execute tracking control, the 6×6 gain matrix $[K]$ must first be propagated backward via a Riccati matrix differential equation (requiring simultaneous backpropagation of the chief orbit and computation of the plant matrix $[A]$), and the six-dimensional costate $\boldsymbol{s}(t)$ must also be backpropagated.

Consider instead that the fundamental solution constants $\boldsymbol{c}$ are used as the state representation, and the desired trajectory to track is natural, thus $\boldsymbol{u}_r = \boldsymbol{0}$ and $\boldsymbol{c}_r(t) = \boldsymbol{c}_r(t_0)$. The state error is $\delta\boldsymbol{c} = \boldsymbol{c} - \boldsymbol{c}_r$ with the following simple dynamics, assuming that the chief orbit is unperturbed:

$$\delta\dot{\boldsymbol{c}} = [B_{\boldsymbol{c}}(t)]\boldsymbol{u} \tag{53}$$

Furthermore, the LQT problem in $\boldsymbol{x}$ space reduces to the linear quadratic regulator problem in $\boldsymbol{c}$ space, with the cost function, the optimal control, and simplified Riccati equation as follows:

$$\tilde{J}_{\mathrm{LQR}} = \frac{1}{2}\delta\boldsymbol{c}(t_f)^{\top}[S]\delta\boldsymbol{c}(t_f) + \frac{1}{2}\int_{t_0}^{t_f}\left(\delta\boldsymbol{c}(t)^{\top}[Q]\delta\boldsymbol{c}(t) + \boldsymbol{u}^{\top}[R]\boldsymbol{u}\right)\mathrm{d}t \tag{54}$$

$$\boldsymbol{u}(t) = -[R]^{-1}[B_{\boldsymbol{c}}]^{\top}[K]\delta\boldsymbol{c}(t) \tag{55}$$

$$[\dot{K}] = [K][B_{\boldsymbol{c}}(t)][R]^{-1}[B_{\boldsymbol{c}}(t)]^{\top}[K] - [Q],\ [K(t_f)] = [S] \tag{56}$$

With this formulation, the controlled $\boldsymbol{x}(t)$ will track natural trajectory $\boldsymbol{x}_r(t)$ through control in $\boldsymbol{c}$ space, where there is no need to backpropagate any costate dynamics; and the Riccati equation is greatly simplified by the absence of an $[A]$ matrix. A complication is that the choice of satisfactory gains is not as straightforward in $\boldsymbol{c}$ space as it is in $\boldsymbol{x}$ space. However, in this paper, the numerical exploration of control using the modal constants is limited to impulsive maneuvers.

C. Impulsive Control Using the Fundamental Solution Constants

The relative motion parameterization in terms of fundamental solution constants is well suited for impulsive maneuver-based control strategies. Returning to Eq. (35), in the absence of disturbances, $[\Omega(t)] = [0_{6\times 6}]$; and the solution for $\boldsymbol{c}$ can be expressed in terms of a series of impulsive maneuvers $\Delta\boldsymbol{v}_i = \Delta\boldsymbol{v}(t_i)$:

$$\boldsymbol{c} = \boldsymbol{c}_0 + \sum_{i=1}^{N}[B_c(t_i)]\Delta\boldsymbol{v}_i \tag{57}$$

Consider the optimal control problem of minimizing the total delta V subject to the dynamics in Eq. (64):

$$J = \sum_{i=1}^{N}\Delta v_i \tag{58}$$

where $\Delta v_i = \|\Delta\boldsymbol{v}(t_i)\|$. Also, let $\Delta\boldsymbol{c} = \boldsymbol{c} - \boldsymbol{c}_0$. Some useful results are borrowed from Ref. [5]. First, consider the sets of control inputs $\boldsymbol{u}(t) \in U$ and the reachable variations $\Delta\boldsymbol{c} \in C$ with costs no greater than J:

$$\mathsf{U}(J) = \left\{\boldsymbol{u}(t)\colon \boldsymbol{u}(t) = \sum_{i=1}^{N}\Delta\boldsymbol{v}_i, \sum_{i=1}^{N}\Delta v_i \le J\right\} \tag{59}$$

$$\mathsf{C}(J) = \left\{\Delta\boldsymbol{c}\colon \Delta\boldsymbol{c} = \sum_{i=1}^{N}[B_c(t_i)]\Delta\boldsymbol{v}_i, \sum_{i=1}^{N}\Delta v_i \le J\right\} \tag{60}$$

As discussed in Ref. [5], the set C is compact and convex, and it scales linearly with J. Furthermore, for a minimum cost $J_{\min}$ to achieve a desired variation, the desired difference in constants $\Delta\boldsymbol{c}^* = \boldsymbol{c}^* - \boldsymbol{c}_0$ lies on the boundary of the set. The minimum delta V to reach this goal in N maneuvers can be obtained in terms of the unit vector $\hat{\boldsymbol{\eta}}$, which is normal to the boundary of C at $\Delta\boldsymbol{c}^*$:

$$J_{\min} = \frac{\hat{\boldsymbol{\eta}}^{\top}\Delta c^*}{\max_{t_i\in[t_0,t_f]}\|\hat{\boldsymbol{\eta}}^{\top}[B_c(t_i)]\|} \tag{61}$$

For integration constant control formulations, Ref. [5] describes a means of numerically obtaining $\hat{\boldsymbol{\eta}}$ using a convex solver, and then linearly solving for an optimal sequence of $N \le n$ impulsive maneuvers for a dynamic system with n state variables. Their approach, which is used in this work, was inspired by Ref. [29] (p. 328, theorem 3), Ref. [30], and Ref. [31] (p. 377, algorithm 1). In general, for the formation-flying problem, a minimum of two maneuvers is required. For the unperturbed problem, only control action induces movement in C: the flow of the integrable dynamics has no effect. This property, combined with the compactness and convexity of C, allows for powerful geometric interpretations for the fuel-optimal impulsive maneuver problem. However, any significant perturbations will play a disruptive role, inducing drifts in $\Delta\boldsymbol{c}$ that would need to be compensated for.

The algorithm for solving for an optimal maneuver sequence is given in the following for the unperturbed problem [5]:

1) Solve the following second-order cone program for the optimal value $\boldsymbol{\eta}^*$:

$$\begin{aligned}&\text{maximize} \quad \tilde{J} = \boldsymbol{\eta}^{\top}\Delta\boldsymbol{c}^*\\ &\text{subject to} \quad \|[B_c(t)]^{\top}\boldsymbol{\eta}\| \le 1 \quad \text{for } t \in [t_0,\ldots,t_j,\ldots,t_f]\end{aligned} \tag{62}$$

where $[t_0, \ldots, t_j, \ldots, t_f] \in \mathbb{R}^k_{\ge 0}$ is a chosen discretization of the control interval.

2) Determine all times $t_i \in [t_0, \ldots, t_j, \ldots, t_f]$ for which $|\|[B_c(t)]^{\top}\boldsymbol{\eta}^*\| - 1| < \epsilon$ for some small numerical precision tolerance $\epsilon \ll 1$. This will yield an N-maneuver sequence, with $N \ll k$, for which the ith impulse is directed along the unit vector:

$$\hat{\boldsymbol{u}}_i = [B_c(t)]^{\top}\boldsymbol{\eta}^* \tag{63}$$

3) The set of delta-V maneuver magnitudes $\{\Delta v_i\}$ needs to satisfy the linear system of equations:

$$\sum_{i=1}^{N}[B_c(t_i)]\hat{\boldsymbol{u}}_i \cdot \Delta v_i = \Delta \boldsymbol{c}^* \tag{64}$$

A traditional relative motion control approach is to use a factorization of the STM to uniquely solve for a two-burn delta-V sequence, given some specified initial and final times. This could also be used with the desired target relative orbit efficiently identified in $\boldsymbol{c}$ space. This $\boldsymbol{c}^*$ would then be mapped to $\boldsymbol{x}^*$ via the fundamental solutions. By necessity, a two-burn solution using either approach will obtain the same answer.

IV. Numerical Results for the Keplerian Case

A. Keplerian Relative Orbit and Its Modes

Consider the example of a bounded relative orbit in the vicinity of an eccentric chief orbit, given by the data listed in Table 1. The specified modal constants $\boldsymbol{c}$ are related to local curvilinear relative states by Eq. (26) using the unity-normalization scheme given by Eq. (27) and its associated discussion. Note that, although $\delta a = 0$, the drift constant c_6 does not exactly equal zero. This is because $\delta a = 0$ is the nonlinear no-drift requirement, and it is not perfectly captured by the linearized no-drift condition. This is a well-known property of linearized solutions; consider, for example, that the linearized no-drift condition for the CW system is $\dot{y} + 2nx = 0$, which only linearly approximates $\delta a = 0$. From the data in Table 1, the resulting Keplerian relative orbit is depicted in 3-D in Fig. 4, and the planar projection appears as a black closed curve in Figs. 5–7.

Figure 5 shows the modal decomposition of the in-plane component of the relative motion using the modes developed in Cartesian coordinates. Figure 6 shows the modal decomposition of the in-plane motion using the modes developed in spherical coordinates and linearly mapped to Cartesian coordinates. For both plots, the initial point of the orbiter and the initial point in each mode are given by dots. Because the relative orbit is nondrifting, the drift mode contribution is zero; thus, the mode appears as a nonmoving point at the origin. For both modal decompositions, the modes shown sum linearly to reproduce the observed relative motion in black. In other words, $\boldsymbol{x}_{2D}(t) = c_1\boldsymbol{\psi}_{2D,1} + c_3\boldsymbol{\psi}_{2D,3} + c_5\boldsymbol{\psi}_{2D,5}$. Recall that the out-of-plane modes (modes 2 and 4) have no in-plane component; they exist only in z, and they are completely decoupled from the in-plane modes.

Comparing Figs. 5 and 6, the spherical coordinate-based modal decomposition reproduces the true relative orbit in a much more straightforward and intuitive manner than the Cartesian coordinate-based counterpart. The motion is represented as a sum of a rectilinear along-track motion (mode 1), a distorted elliptical motion (mode 3), and the offset circular trajectory (mode 5). This is the simplest geometric representation possible for Keplerian relative motion, with two of the three bounded in-plane motions given as basic shapes.

Because the fundamental modal motions only need to be computed once, variations in the relative motion due to changes in the modal constants can be explored with a minimal amount of numerical computation. For example, exploring a range of variations in c_1, Fig. 7 is produced. The initial ($t = t_0$) and midorbit ($t = t_0 + (T/2)$) points are denoted with dots and with an "x," respectively; and the original relative orbit is given in black. The effect of isolated changes in c_1 is to shift the motion further along in the along-track direction as c_1 is increased, with the additional effect of rotating and distorting the planar component of the relative orbit. Note that the x scale of the relative orbit is not affected at all. Similar figures can be generated to isolate the effects of changes in c_3 and c_5 on the relative orbit shape

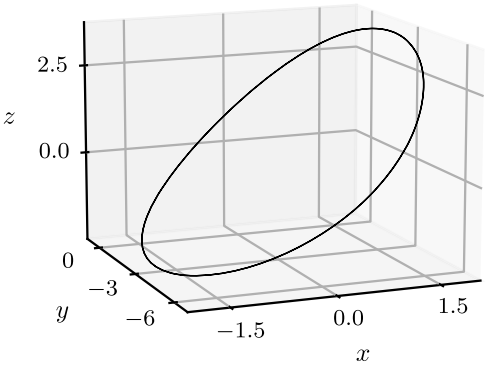

Fig. 4 Example relative orbit.

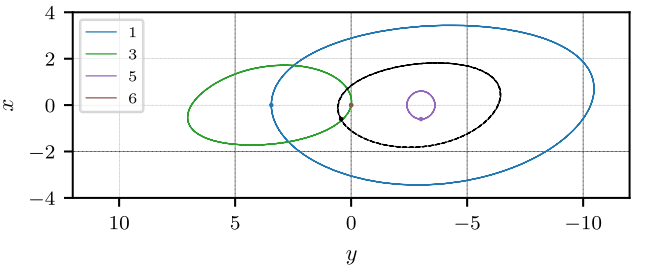

Fig. 5 Cartesian planar modes.

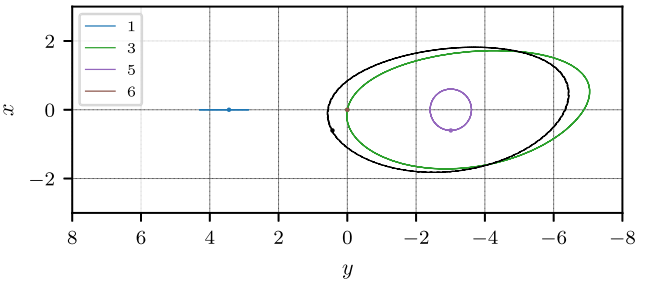

Fig. 6 Spherical planar modes.

and location. However, changing the scales of c_3 and c_5 also changes the size of the relative orbit. To display the characteristic changes in relative orbits with these parameters clearly on individual plots, the relative orbits are computed across desired ranges for these parameters, as was done for Fig. 7; then, the orbits are rescaled such that $\|\boldsymbol{c}_{\text{new}}\| = \|\boldsymbol{c}_{\text{old}}\|$ to preserve the original relative orbit scale. The resulting plots are given in Fig. 8 for variations in c_3 and Fig. 9 for variations in c_5.

In Fig. 8, as c_3 is decreased from its original value of 7.07, the rescaled relative orbit shifts from the original relative orbit (given in black), to more centered and symmetric relative motion in the middle of the range (near $c_3 = 0$), to an essentially reversed version of the original for $c_3 < 0$. Note that there would also be accompanying relative orbit scale changes with the changing value of c_3, but the rescaled orbit plot sacrifices this information to better show the variations in the relative orbit geometry. Figure 9 shows the variations in the rescaled relative orbit due to changes in c_5, with an original

Table 1 Simulation parameters

Parameter	Value
Chief orbit elements	$\boldsymbol{\alpha} = (a, e, i, \Omega, \omega, f_0) = (8600\text{ km}, 0.2, 25\text{ deg}, 0\text{ deg}, 270.001\text{ deg}, 90\text{ deg})$
Deputy relative orbit	$\delta\boldsymbol{\alpha} = \boldsymbol{\alpha}_d - \boldsymbol{\alpha}_c = (0.0, 0.0002, 0.02\text{ deg}, 0\text{ deg}, 0\text{ deg}, 0.003\text{ deg})$
Modal constants	$\boldsymbol{c} = (4.3, 0.0, 7.07, 3.60, 3.61, -0.014)$

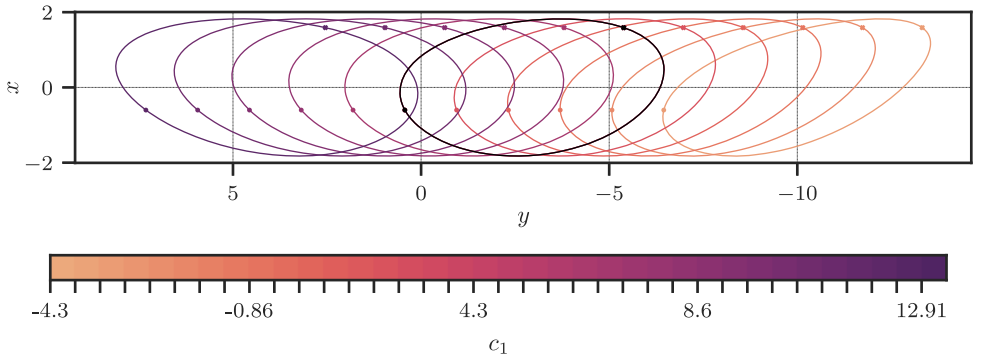

Fig. 7 Variations of the planar relative motion with c_1.

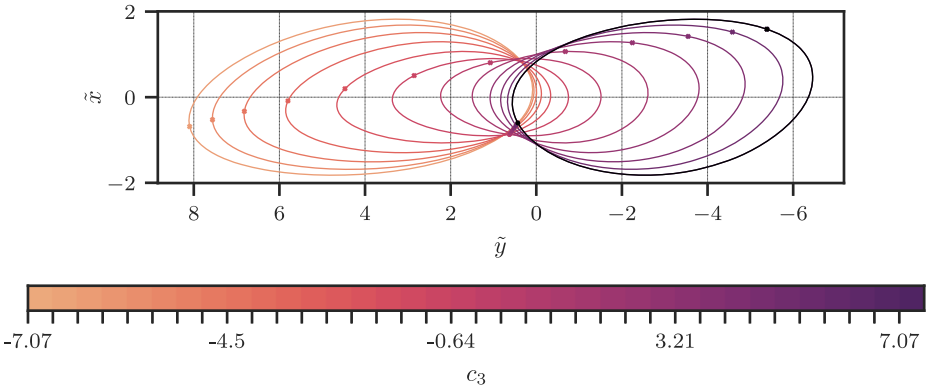

Fig. 8 Variations of the planar relative motion with c_3 (rescaled).

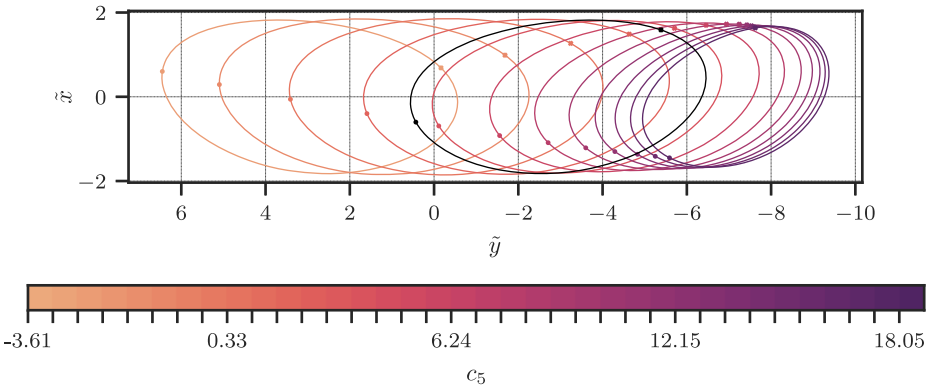

Fig. 9 Variations of the planar relative motion with c_5 (rescaled).

value of $c_5 = 3.61$. The negative value is essentially flipped about the x axis; and as the value is increased, the rescaled relative orbits gradually circularize as the contribution of circular mode 5 is increased in relative scale.

Figures 7–9 show that the parameter space for the in-plane component of bounded relative orbits is only three-dimensional. The two out-of-plane modes add an additional two dimensions, completely decoupled from the in-plane design. From the perspective of the modal constants, it is conceptually easy and numerically efficient for the astrodynamicist to explore all possible useful types of relative motion that can exist. In this manner, the vector of modal constants $\boldsymbol{c}$ serves as the design space, and it uniquely determines the relative motion state when combined with a given time since epoch $t - t_0$. As discussed earlier, it is also possible to compute how the constants vary under the influence of non-Keplerian dynamics. With such a study, the influence of perturbations on relative motion can be viewed as an evolving alteration of the relative scales of the constituent Keplerian relative motion modes that form the basis for the unperturbed problem.

B. Effects of Perturbations: Modeling with J_2

To demonstrate the behavior of the Keplerian modal constants under the influence of perturbations, consider the ubiquitous example of J_2-perturbed relative motion, which is highly relevant for Earth orbits. To compute the perturbed dynamics of the Keplerian modal constants, Eq. (31) is used, with equations from Ref. [24] providing the linearized perturbed relative motion dynamics; and it evaluated using the following equations for the acceleration, differential acceleration, and jerk induced by the J_2-perturbed Keplerian dynamics:

$$\ddot{\boldsymbol{r}} = -\frac{\mu}{r^3}\boldsymbol{r} - \frac{3\mu J_2 R^2}{2r^4}\left((1-5(\hat{\boldsymbol{r}}\cdot\hat{\boldsymbol{K}})^2)\hat{\boldsymbol{r}} + 2(\hat{\boldsymbol{r}}\cdot\hat{\boldsymbol{K}})\hat{\boldsymbol{K}}\right) \tag{65}$$

$$\nabla_{\boldsymbol{r}}\ddot{\boldsymbol{r}} = -\frac{3\mu J_2 R^2}{2r^5}\Big[(1-5(\hat{\boldsymbol{K}}\cdot\hat{\boldsymbol{r}})^2)I + 2\hat{\boldsymbol{K}}\,\hat{\boldsymbol{K}}^{\top} + 5(7(\hat{\boldsymbol{K}}\cdot\hat{\boldsymbol{r}})^2 - 1)\hat{\boldsymbol{r}}\,\hat{\boldsymbol{r}}^{\top} - 10(\hat{\boldsymbol{K}}\cdot\hat{\boldsymbol{r}})(\hat{\boldsymbol{K}}\,\hat{\boldsymbol{r}}^{\top} + \hat{\boldsymbol{r}}\,\hat{\boldsymbol{K}}^{\top})\Big] \tag{66}$$

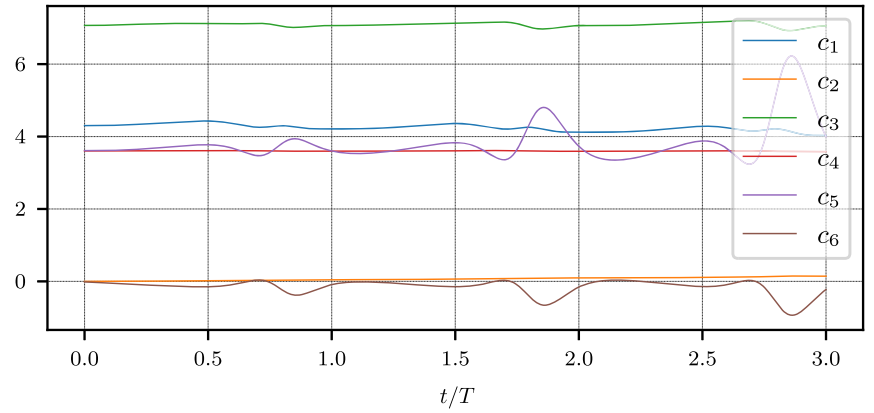

Fig. 10 Variation of modal constants with J_2.

$$\ddot{\boldsymbol{r}} = (\nabla_{\boldsymbol{r}}\ddot{\boldsymbol{r}})\dot{\boldsymbol{r}} \tag{67}$$

where $\hat{\boldsymbol{K}}$ denotes the polar axis unit vector, R is the equatorial radius, I is the 3×3 identity matrix, and $\hat{\boldsymbol{r}} = \boldsymbol{r}/r$. The dynamics given by Eq. (31) are integrated in parallel with the J_2-perturbed chief orbit.

The same initial chief orbit and deputy relative orbit conditions from Table 1 are selected but with Earth's J_2 perturbation active. As a result of this perturbation, variations are induced in the Keplerian modal constants. Figure 10 shows the resulting behavior in $\boldsymbol{c}$ for three unperturbed chief orbit periods. The effect of J_2 is limited to small oscillations in the modal constants, but these oscillations grow over time, which is an unfortunate but unavoidable property. For the case of J_2, it seems that the modified orbital frequency due to the perturbation requires that the secular drift mode (mode 6) be used to fully describe the perturbed state. This is because all other modes are periodic on the interval $[0, T]$, and variations in their sums would be unable to describe a relative orbit on the shortened interval $[0, T - \Delta T_{J_2}]$. Additionally, the J_2 perturbation induces slow long-term drift in the relative orbit. The drift mode is used to describe the perturbed solution, and it grows and shifts over time; so, variations in other modes (primarily mode 5) are induced to compensate for these variations. This yields the opposing behaviors of c_5 and c_6 seen in Fig. 10. Despite these growing oscillations, the long-term drift in c_5 and c_6, as well as in the other c_i parameters, is quite slow. The averaged dynamics in $\boldsymbol{c}$ could thus be a useful lens for studying relative motion in the perturbed problem, especially for even zonal harmonics like J_2, but such a study is not explored here. Lastly, the growing oscillations are not a major problem for modeling because the fundamental solutions can always be reinitialized as needed.

C. Impulsive Maneuver Control Examples: Keplerian Orbit

To demonstrate unperturbed control using the Keplerian modal constants, consider the problem of changing from the initial relative motion dictated by the data in Table 1 to a new planar nondrifting

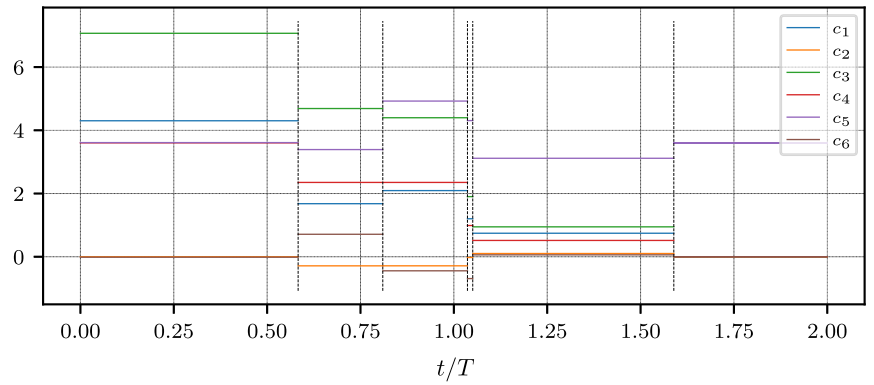

Fig. 11 Five-burn maneuver: modal constants.

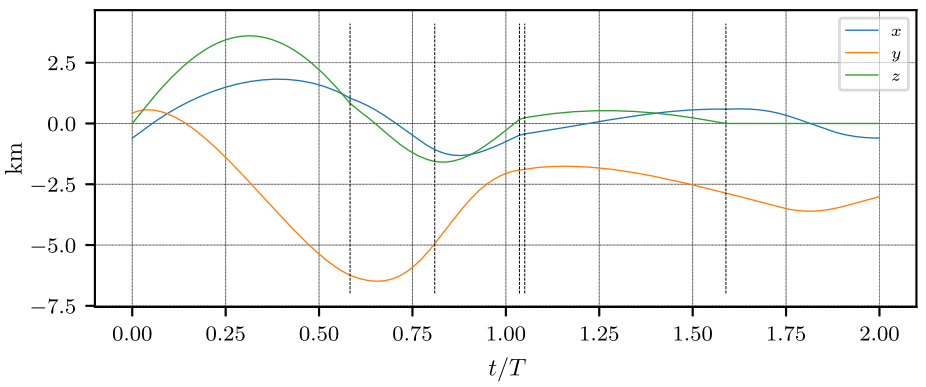

Fig. 12 Five-burn maneuver: local Cartesian coordinates.

relative orbit parameterized by $c_5 = 3.61$. To implement this test, the previously discussed impulsive maneuver-based control solution strategy is implemented in Python using cvxpy. For this impulsive control example with the Keplerian case, time is discretized into 100 points on the interval of $t_i \in [t_0 + 1, 590.6\text{ s}, t_0 + 12, 724.7\text{ s}]$. Thus, the number of constraints given by Eq. (62) is 100. This does not stress the solver, and the optimal maneuver sequence is found quite quickly. The resulting impulsive control solution consists of five maneuvers for a combined delta V of only 2.7 m/s, as compared to 7.0 m/s for a two-burn transfer in the same interval. The changes in $\boldsymbol{c}$ with each maneuver are plotted in Fig. 11, with vertical lines indicating each maneuver. The relative position components are plotted in Fig. 12. The initial, transfer, and final relative motions are shown in 3-D in Fig. 13. The initial relative orbit is the large blue closed curve, and the final relative orbit is the small orange planar circular trajectory. The transfer trajectory is given by the dashed black line, and the maneuver points are indicated with red dots. The chief location is indicated by a star.

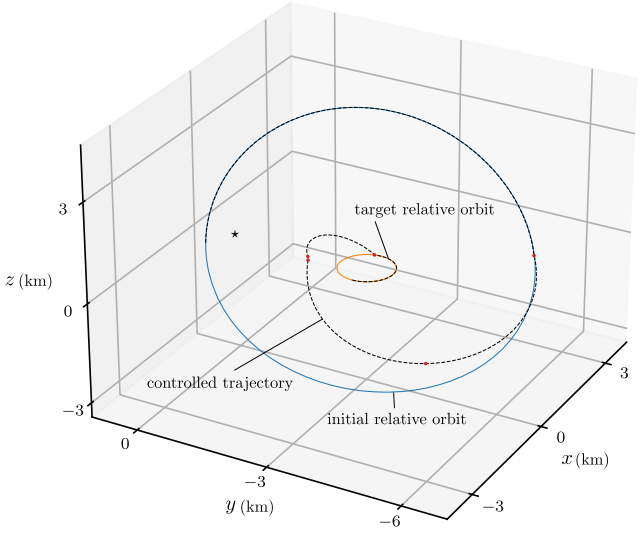

Fig. 13 Relative orbit transfer using the modal constants.

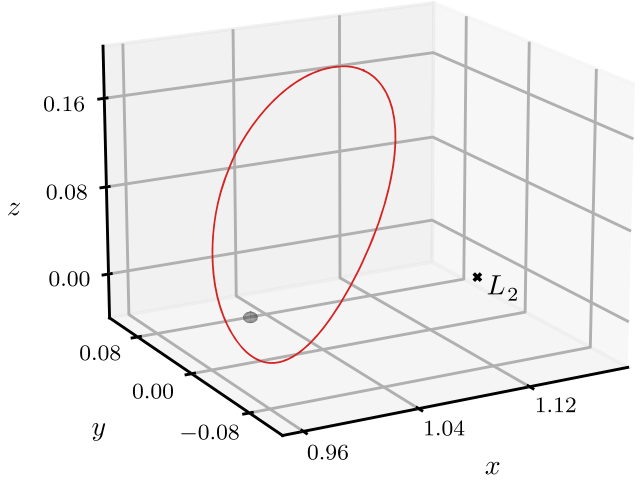

Fig. 14 Stable L_2 halo orbit.

Control using the modal solution constants is highly convenient due to both the straightforward geometric interpretation of the c_i parameters and the efficient means by which multimaneuver impulsive control schedules can be obtained. This is demonstrated by the preceding simple examples with Keplerian dynamics. However, extending this control design to account for the effect of perturbations on $\boldsymbol{c}$ is necessary for elegant flight implementation: particularly for long-duration control maneuver sequences. This will be explored in future work, but mitigating the effects of perturbations in control design in $\boldsymbol{c}$ space should be straightforward because even in the perturbed relative motion case, the $\boldsymbol{c}$ parameters do not lose their geometric meaning. This is highly convenient, and it generally does not hold for most other perturbed integral representations. For example, for relative motion parameterizations using orbit element differences of $\delta\boldsymbol{\alpha} = \boldsymbol{\alpha}_d - \boldsymbol{\alpha}_c$, the perturbations modify $\boldsymbol{\alpha}_c$; as a result, the resulting exact local coordinate behavior mapped from a particular desired $\delta\boldsymbol{\alpha}$ changes over time.

V. Numerical Examples for the CR3BP Case

Consider a stable northern L_2 halo orbit with an orbit period of $T = 9.504$ days. This orbit is given in Fig. 14. For this orbit, there are four center modes and two trivial modes ($\boldsymbol{\psi}_1$ and $\boldsymbol{\psi}_2$) in its vicinity. The center modes are composed of incommensurate frequencies, and so they trace out complex shapes over long time spans. This is demonstrated with plots of $\boldsymbol{\psi}_3$ and $\boldsymbol{\psi}_5$ propagated with the linearized dynamics for 240 chief orbits, given by Fig. 15. The scale shown corresponds to relative motion on the kilometer scale, but it is plotted in the dimensionless CR3BP length scale. The dimensionless frequencies are $\omega_1 = 1.2511$ and $\omega_2 = 0.7604$. Not shown is the trivial mode, which traces a closed curve with each chief orbit. Note that the chief location is plotted with a star.

As a demonstration of the impulsive control strategy discussed earlier, consider the control case summarized in Table 2. The modal constants $\boldsymbol{c}$ are related to the relative state in nondimensional CR3BP coordinates via Eqs. (43) and (44) using the unity-normalization scheme given by Eq. (27) and its associated discussion. The initial motion is bounded but irregular, and the bounded trivial mode is targeted. The resulting relative motion is plotted in Fig. 16. The uncontrolled trajectory is given in blue for two chief orbits; the target trajectory is in orange; and the controlled trajectory is given by the

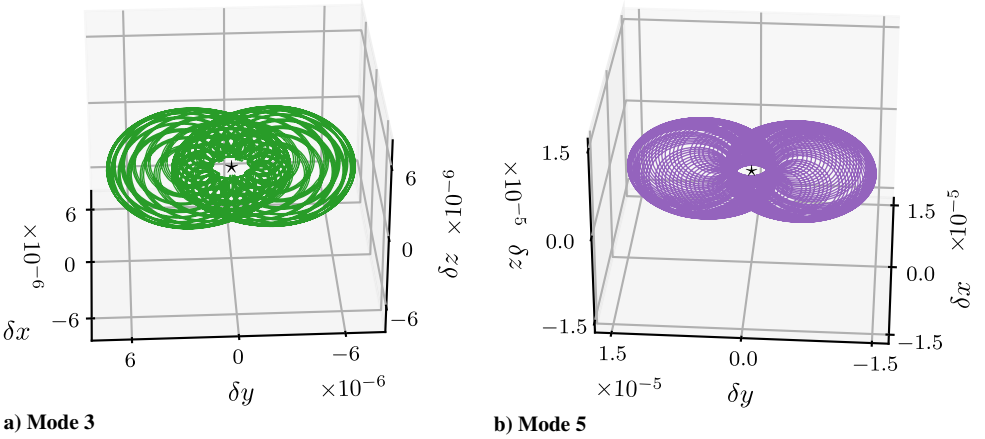

a) Mode 3 **b) Mode 5**

Fig. 15 Center modes: stable L_2 northern halo orbit.

Table 2 Halo orbit control simulation parameters (stable orbit example)

Parameter	Value
Initial relative motion	$\boldsymbol{c}_0 = (0, 0, 0.2, 0.1, 0.08, 0)\alpha$, $\alpha = 5.2 \times 10^{-6}$
Initial state	$\delta\boldsymbol{x}_0 = (-0.01, 0.309, -0.005, 0.168, -0.002, 0.362)\alpha$
Desired relative motion	$\boldsymbol{c}^* = (0.2, 0, 0, 0, 0, 0)\alpha$
Maneuver interval	$\tau \in [1.23, 3.29]$
Maneuver times	$\tau_1 = 1.37$, $\tau_2 = 2.876$, $\tau_3 = 3.013$
Resulting maneuvers	$\Delta\boldsymbol{v}_1 = (-0.281, 0.094, 0.161)\alpha$
	$\Delta\boldsymbol{v}_2 = (-0.131, -0.027, 0.085)\alpha$
	$\Delta\boldsymbol{v}_3 = (-0.221, -0.064, 0.121)\alpha$

Table 3 Halo orbit control simulation parameters: example 2(a)

Parameter	Value
Initial relative motion	$\boldsymbol{c}_0 = (0, 0, 0, 0, 0, 0)$
Initial state	$\delta\boldsymbol{x}_0 = (0, 0, 0, 0, 0, 0)$
Desired relative motion	$\boldsymbol{c}^* = (0, 0, 0.3, 0, 0, 0)\alpha$, $\alpha = 5.2 \times 10^{-6}$
Maneuver interval	$\tau \in [1.90, 5.08]$
Maneuver times	$\tau_1 = 1.903$, $\tau_2 = 2.538$, $\tau_3 = 3.595$, $\tau_4 = 3.807$, $\tau_5 = 4.864$
Resulting maneuvers	$\Delta\boldsymbol{v}_1 = (-0.035, -0.007, 0.052)\alpha$
	$\Delta\boldsymbol{v}_2 = (-0.148, 0.278, 0.052)\alpha$
	$\Delta\boldsymbol{v}_3 = (0.028, 0.002, -0.068)\alpha$
	$\Delta\boldsymbol{v}_4 = (0.028, -0.035, -0.101)\alpha$
	$\Delta\boldsymbol{v}_5 = (-0.001, 0, 0.0005)\alpha$

dashed line, with impulsive maneuver points marked by red dots. The chief is shown as a star. This figure is plotted in the rotating CR3BP coordinates, and not the LVLH frame. The figure shows that the impulsive maneuver-based control strategy is successful in achieving the desired relative motion.

Next, consider two cases of control near an unstable L_2 halo orbit. This is a northern L_2 halo orbit with a period of $T = 14.676$ days. For this orbit, there are the trivial bounded and drift modes $\boldsymbol{\psi}_1$ and $\boldsymbol{\psi}_2$, two center modes $\boldsymbol{\psi}_3$ and $\boldsymbol{\psi}_4$, a stable mode $\boldsymbol{\psi}_5$, and an unstable mode $\boldsymbol{\psi}_6$. The center mode $\boldsymbol{\psi}_3$ is propagated for many orbits and given in Fig. 17. Its dimensionless frequency is $\omega_1 = 0.1288$.

For this unstable halo orbit, two relative motion control examples are briefly highlighted. The first is control from the chief point of $\delta\boldsymbol{x} = \boldsymbol{0}$ to the target one of the center modes. The second is an example of regulation from the trivial mode to the chief point. Starting with the example given by Table 3 and Fig. 18, the initial point is at $\delta\boldsymbol{x} = \boldsymbol{0}$ and the target motion is in orange. The controlled trajectory is given by the dashed line, and the control maneuvers are labeled on the plot with red points. The control successfully targets the quasi-periodic mode $\boldsymbol{\psi}_3$, but a small residual error projected into the unstable subspace results in a subsequent need for correction; so, the trajectory departs from the target mode. This is a fundamental property of relative motion control in the vicinity of an unstable halo orbit: corrective maneuvers will always be necessary on some timescale, due to the combined effects of nonlinearity and instability.

The second example is given by the data in Table 4 and the trajectory in Fig. 19. The initial trivial modal motion is given in blue, the controlled trajectory is given by the dashed line, and the control maneuvers are labeled with red dots. This example demonstrates

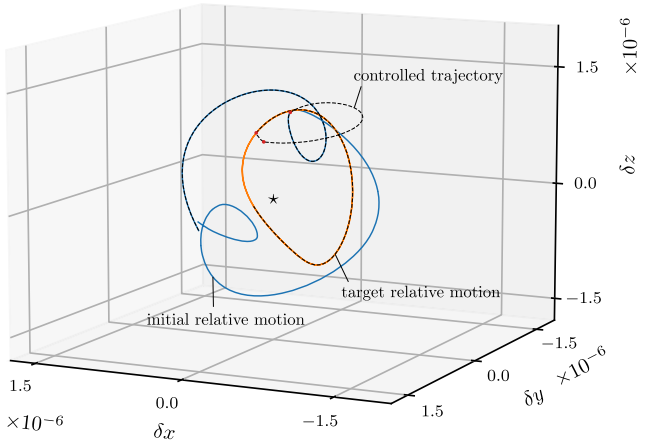

Fig. 16 Relative motion with impulsive control: stable L_2 halo orbit.

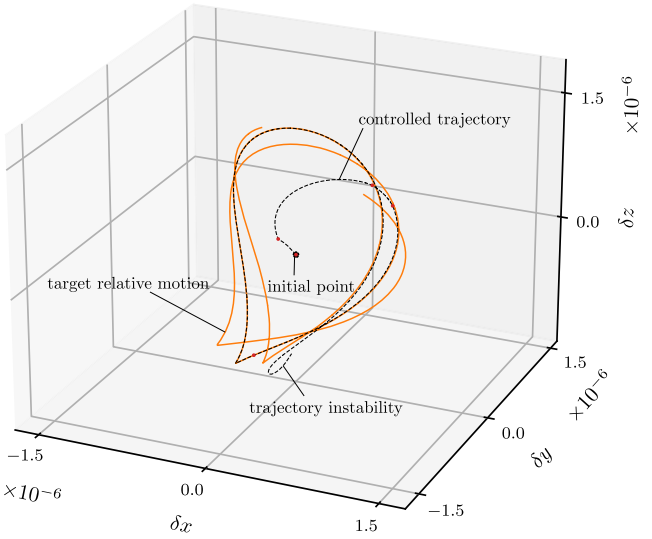

Fig. 18 Control to center mode: unstable L_2 halo orbit.

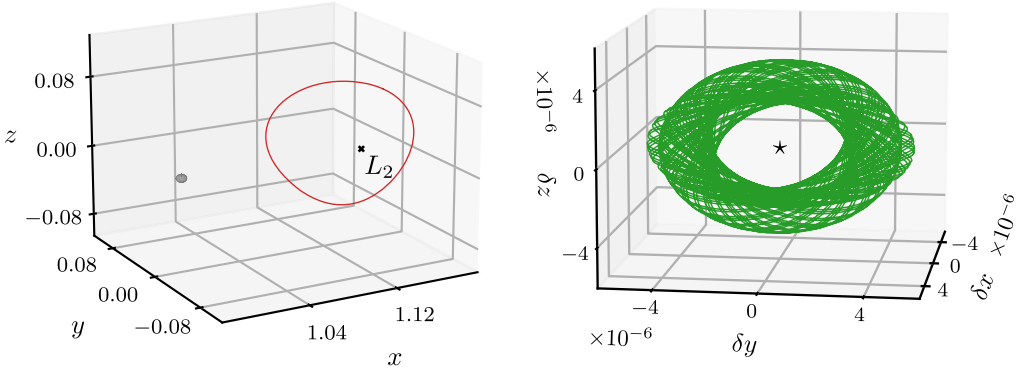

a) Halo orbit: example 2(a) **b) Center mode**

Fig. 17 Unstable L_2 northern halo orbit and a center mode.

Table 4 Halo orbit control simulation parameters: example 2(b)

Parameter	Value
Initial relative motion	$\boldsymbol{c}_0 = (0.2, 0, 0, 0, 0, 0)\alpha$, $\alpha = 5.2 \times 10^{-6}$
Initial state	$\delta\boldsymbol{x}_0 = (0, -0.127, 0, -0.117, 0, -0.1)\alpha$
Desired relative motion	$\boldsymbol{c}^* = (0, 0, 0, 0, 0, 0)$
Maneuver interval	$\tau \in [1.90, 5.08]$
Maneuver times	$\tau_1 = 1.903$, $\tau_2 = 2.538$, $\tau_3 = 2.749$, $\tau_4 = 4.018$, $\tau_5 = 4.230$, $\tau_6 = 4.864$
Resulting maneuvers	$\Delta\boldsymbol{v}_1 = (-0.008, 0.0005, -0.004)\alpha$
	$\Delta\boldsymbol{v}_2 = (-0.002, -0.003, 0.002)\alpha$
	$\Delta\boldsymbol{v}_3 = (-0.044, 0.084, 0.081)\alpha$
	$\Delta\boldsymbol{v}_4 = (-0.045, -0.086, 0.081)\alpha$
	$\Delta\boldsymbol{v}_5 = (-0.0007, -0.001, 0.0006)\alpha$
	$\Delta\boldsymbol{v}_6 = (-0.008, -0.0004, -0.004)\alpha$

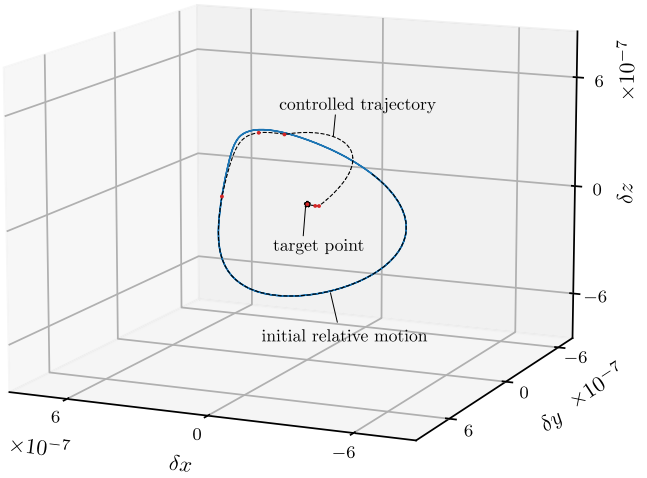

Fig. 19 Regulation to periodic orbit: unstable L_2 halo orbit.

regulation control in this environment, with the chief at $\delta\boldsymbol{x} = \boldsymbol{0}$ successfully targeted to a high degree of numerical precision. A similar strategy could be used for orbit regulation, keeping the spacecraft on the unstable periodic orbit.

VI. Future work

The possibilities for future work are extensive. The modal decomposition procedure could be computed in coordinates with superior linearization, yielding a larger region of validity. Additionally, an alternate choice of coordinates for relative motion in the CR3BP could yield greater geometric insight than the standard rotating coordinates used in this work, particularly for the center modes. The current methodology is only applicable to motion in the vicinity of periodic orbits. A perturbative application of the modal decomposition procedure (explored in early work in Ref. [32]) could extend the methods and control techniques discussed in this paper to more a realistic setting of motion in the vicinity of a satellite orbit that roughly repeats but is not periodic, e.g., any orbit for which the chief state $\boldsymbol{X}(t) \approx \boldsymbol{X}(t + T)$ for some time T. This is achieved by finding the nearest T-periodic LTV system to a given linearization and using the modal decomposition from the former to approximately describe the motion in the latter. Additionally, for motion in the vicinity of a general quasi-periodic orbit, the periodic Lyapunov–Floquet reducing transformation is replaced with a quasi-periodic Lyapunov–Perron transformation, which can be challenging to compute. Reference [33] is relevant to this. If the reducing transformation for the quasi-periodic case can be computed efficiently, the modal decomposition methodology will be extended quite naturally to general orbits in the full zonal problem and quasi-periodic orbits in the restricted three-body problems.

VII. Conclusions

This paper introduces the method of fundamental modal solutions for designing, analyzing, and controlling satellite relative motion in the vicinity of general periodic orbits. The close-proximity satellite relative motion is given as a linear sum of fundamental modal solutions weighed by the modal constants. This facilitates highly simplified geometric exploration of the satellite relative motion problem. Using a variation-of-parameters approach, the modal constants also serve as a rigorous state representation for the perturbed and/or controlled satellite relative state. The representation for perturbed relative motion is tested with the commonly studied J_2 problem. For the unperturbed problem of satellite relative motion control, the modal constants have null dynamics but are steered in time-varying directions by control. This is a highly beneficial property for control design (especially impulsive control), and this paper demonstrates the use of modal constants to simplify the control problem using previously established techniques for general integration constant formulations for dynamical systems.

The procedure applied analytically to the Keplerian relative motion problem can also be applied numerically to other dynamical situations that admit periodic orbits, and this is demonstrated with application to the classical circular restricted three-body problem. Highly fuel-efficient impulsive transfer examples are computed using the same procedure as was used for the Keplerian case in a manner that is also highly numerically efficient. This has many applications. First, it lays the groundwork for computationally efficient onboard close-proximity satellite relative motion transfers in the cislunar environment. The procedure can also be applied in another highly relevant problem, known as the augmented normalized Hill three-body problem, to explore efficient satellite relative motion control in terminator orbits around asteroids.

References

[1] Schaub, H., and Junkins, J. L., *Analytical Mechanics of Space Systems*, 4th ed., AIAA Education Series, AIAA, Reston, VA, 2018. https://doi.org/10.2514/4.105210

[2] Butcher, E. A., Burnett, E. R., and Lovell, T. A., "Comparison of Relative Orbital Motion Perturbation Solutions in Cartesian and Spherical Coordinates," *AAS/AIAA Spaceflight Mechanics Meeting*, AAS Paper 17-202, Univelt, Inc., Escondido, CA, 2017.

[3] Schaub, H., "Relative Orbit Geometry Through Classical Orbit Element Differences," *Journal of Guidance, Control, and Dynamics*, Vol. 27, No. 5, 2004, pp. 839–848. https://doi.org/10.2514/1.12595

[4] D'Amico, S., and Montenbruck, O., "Proximity Operations of Formation-Flying Spacecraft Using an Eccentricity/Inclination Vector Separation," *Journal of Guidance, Control, and Dynamics*, Vol. 29, No. 3, 2006, pp. 554–563. https://doi.org/10.2514/1.15114

[5] Guffanti, T., and D'Amico, S., "Integration Constants as State Variables for Optimal Path Planning," *2018 European Control Conference (ECC)*, Inst. of Electrical and Electronics Engineers, New York, 2018, pp. 1–6. https://doi.org/10.23919/ECC.2018.8550448

[6] D'Amico, S., Ardaens, J. S., and Larsson, R., "In-Flight Demonstration of Formation Control Based on Relative Orbit Elements," *4th International Conference on Spacecraft Formation Flying Missions and Technologies*, 2011, https://www.semanticscholar.org/paper/In-flight-demonstration-of-formation-control-based-D'Amico-Ardaens/7fef115b2180703cf27c4afcf733db0fc95c8b0d.

[7] Schaub, H., and Alfriend, K. T., "Hybrid Cartesian and Orbit Element Feedback Law for Formation Flying Spacecraft," *Journal of Guidance, Control, and Dynamics*, Vol. 25, No. 2, 2002, pp. 387–393. https://doi.org/10.2514/2.4893

[8] Sinclair, A. J., Sherrill, R. E., and Lovell, T. A., "Calibration of Linearized Solutions for Satellite Relative Motion," *Journal of Guidance, Control, and Dynamics*, Vol. 37, No. 4, 2014, pp. 1362–1367. https://doi.org/10.2514/1.G000037

[9] Bennett, T., and Schaub, H., "Continuous-Time Modeling and Control Using Nonsingular Linearized Relative-Orbit Elements," *Journal of Guidance, Control, and Dynamics*, Vol. 39, No. 12, 2016, pp. 2605–2614. https://doi.org/10.2514/1.G000366

[10] Clohessy, W. H., and Wiltshire, R. S., "Terminal Guidance System for Satellite Rendezvous," *Journal of the Aerospace Sciences*, Vol. 27,

No. 9, 1960, pp. 653–658.
https://doi.org/10.2514/8.8704

[11] Liou, J.-C., "An Active Debris Removal Parametric Study for LEO Environment Remediation," *Advances in Space Research*, Vol. 47, No. 11, 2011, pp. 1865–1876.
https://doi.org/10.1016/j.asr.2011.02.003

[12] Sullivan, J., Grimberg, S., and D'Amico, S., "Comprehensive Survey and Assessment of Spacecraft Relative Motion Dynamics Models," *Journal of Guidance, Control, and Dynamics*, Vol. 40, No. 8, 2017, pp. 1837–1859.
https://doi.org/10.2514/1.G002309

[13] Burnett, E. R., and Schaub, H., "Geometric Perspectives on Fundamental Solutions in the Linearized Satellite Relative Motion Problem," *Acta Astronautica*, Vol. 190, Jan. 2022, pp. 48–61.
https://doi.org/10.1016/j.actaastro.2021.09.028

[14] Nayfeh, A. H., and Mook, D. T., *Nonlinear Oscillations*, Wiley, New York, 1979.
https://doi.org/10.1002/9783527617586

[15] Sherrill, R. E., Sinclair, A. J., Sinha, S. C., and Lovell, T. A., "Lyapunov–Floquet Control of Satellite Relative Motion in Elliptic Orbits," *IEEE Transactions on Aerospace and Electronic Systems*, Vol. 51, No. 4, Oct. 2015, pp. 2800–2810.
https://doi.org/10.1109/TAES.2015.140281

[16] Koenig, A. W., Guffanti, T., and D'Amico, S., "New State Transition Matrices for Spacecraft Relative Motion in Perturbed Orbits," *Journal of Guidance, Control, and Dynamics*, Vol. 40, No. 7, 2017, pp. 1749–1768.
https://doi.org/10.2514/1.G002409

[17] Gaias, G., and Lovera, M., "Trajectory Design for Proximity Operations: The Relative Orbital Elements' Perspective," *Journal of Guidance, Control, and Dynamics*, Vol. 44, No. 2, 2021, pp. 2294–2302.
https://doi.org/10.2514/1.G006175

[18] Gómez, G., Howell, K., Masdemont, J., and Simó, C., "Station-Keeping Strategies for Translunar Libration Point Orbits," *AAS/AIAA Spaceflight Mechanics Meeting*, American Astronautical Soc. Paper 98-168, Springfield, VA, 1998.

[19] Howell, K. C., and Marchand, B. G., "Natural and Non-Natural Spacecraft Formations near the L1 and L2 Libration Points in the Sun–Earth/Moon Ephemeris System," *Dynamical Systems*, Vol. 20, No. 1, 2005, pp. 149–173.
https://doi.org/10.1080/1468936042000298224

[20] D'Amico, S., "Relative Orbital Elements as Integration Constants of Hill's Equations," DLR, German Aerospace Center TR DLR-GSOC TN 05-08, Weissling, Germany, 2005.

[21] Sullivan, J., and D'Amico, S., "Nonlinear Kalman Filtering for Improved Angles-Only Navigation Using Relative Orbital Elements," *Journal of Guidance, Control, and Dynamics*, Vol. 40, No. 9, 2017, pp. 2183–2200.
https://doi.org/10.2514/1.G002719

[22] Alfriend, K. T., Vadali, S. R., Gurfil, P., How, J. P., and Breger, L. S., *Spacecraft Formation Flying*, Elsevier, Oxford, England, U.K., 2010.
https://doi.org/10.1016/C2009-0-17485-8

[23] Guffanti, T., and D'Amico, S., *Multi-Agent Passive Safe Optimal Control Using Integration Constants as State Variables*, AIAA, Reston, VA, 2021.
https://doi.org/10.2514/6.2021-1101

[24] Casotto, S., "The Equations of Relative Motion in the Orbital Reference Frame," *Celestial Mechanics and Dynamical Astronomy*, Vol. 124, No. 3, 2016, pp. 215–234.
https://doi.org/10.1007/s10569-015-9660-1

[25] Richardson, D. L., and Mitchell, J. W., "A Third-Order Analytical Solution for Relative Motion with a Circular Reference Orbit," *Journal of the Astronautical Sciences*, Vol. 51, No. 1, 2003, pp. 1–12.
https://doi.org/10.1007/BF03546312

[26] Koon, W. S., Lo, M. W., Marsden, J. E., and Ross, S. D., *Dynamical Systems, The Three-Body Problem, and Space Mission Design*, Marsden Books, Wellington, New Zealand, 2006.

[27] Nayfeh, A., *Perturbation Methods*, Wiley, New York, 2000.
https://doi.org/10.1002/9783527617609

[28] Hinch, E. J., *Perturbation Methods*, Cambridge Univ. Press, Cambridge, England, U.K., 1991.
https://doi.org/10.1017/CBO9781139172189

[29] Lee, E. B., and Markus, L., *Foundations of Optimal Control Theory*, Wiley, New York, 1967, p. 328.

[30] Gilbert, E., and Harasty, G., "A Class of Fixed-Time Fuel-Optimal Impulsive Control Problems and an Efficient Algorithm for their Solution," *IEEE Transactions on Automatic Control*, Vol. 16, No. 1, 1971, pp. 1–11.
https://doi.org/10.1109/TAC.1971.1099656

[31] Arzelier, D., Bréhard, F., Deak, N., Joldes, M., Louembet, C., Rondepierre, A., and Serra, R., "Linearized Impulsive Fixed-Time Fuel-Optimal Space Rendezvous: A New Numerical Approach," *IFAC-PapersOnLine*, Vol. 49, No. 17, 2016, pp. 373–378.
https://doi.org/10.1016/j.ifacol.2016.09.064

[32] Burnett, E., and Schaub, H., "Modal Decomposition of Spacecraft Relative Motion in Quasi-Periodic Orbits," *AAS/AIAA Astrodynamics Specialist Conference*, American Astronautical Soc. Paper 20-506, Springfield, VA, 2020.

[33] Jorba, À., "Numerical Computation of the Normal Behaviour of Invariant Curves of n-Dimensional Maps," *Nonlinearity*, Vol. 14, No. 5, 2001, pp. 943–976.
https://doi.org/10.1088/0951-7715/14/5/303